ABSTRACT

REECE, STEPHEN MALO. Primary and Photochemically Aged Aerosol Emissions from Biomass Cookstoves: Chemical and Physical Characterization. (Under the direction of Dr. Andrew Grieshop).

Secondary organic aerosol (SOA) formation during photo-oxidation of primary emissions from cookstoves used in developing countries may make important contributions to their climate and air quality impacts. We present results from laboratory experiments with a field portable oxidation flow reactor (F-OFR) to study the evolution of emissions over hours to weeks of equivalent atmospheric aging. Lab tests measured fresh and aged emissions from a 3 stone fire (TSF), a "rocket" natural draft stove (NDS) and a forced draft gasifier stove (FDGS), in order of increasing modified combustion efficiency (MCE) and decreasing particulate matter emission factors (EF). SOA production was observed for all stoves/tests; organic aerosol (OA) enhancement factor ranged from 1.2 to 3.1, decreasing with increased MCE. In primary emissions, OA mass spectral fragments associated with oxygenated species (primary biomass burning markers) increased (decreased) with MCE; fresh OA from FDGS combustion was especially oxygenated. OA oxygenation increased with further oxidation for all stove emissions, even where minimal enhancement was observed. More efficient stoves emit particles with greater net direct specific warming than TSFs, with the difference increasing with aging. Our results show that the properties and evolution of cookstove emissions are a strong function of combustion efficiency and atmospheric aging.

Primary and Photochemically Aged Aerosol Emissions from Biomass Cookstoves: Chemical and Physical Characterization

by
Stephen Malo Reece

A thesis submitted to the Graduate Faculty of
North Carolina State University
in partial fulfillment of the
requirements for the degree of
Master of Science

Civil Engineering

Raleigh, North Carolina

2017

APPROVED BY:

Dr. Andrew P. Grieshop
Committee Chair

Dr. Markus D. Petters

Dr. Fernando Garcia Menendez

BIOGRAPHY

Stephen Malo Reece was born in Jacksonville, Florida on November 23, 1991. He was raised in Hampstead, North Carolina, where he attended the Topsail school district and then transferred to the Pender Early College where he earned an Associate’s Degree at Cape Fear Community College. In 2010, Stephen was accepted into North Carolina State University where he decided to major in Environmental Engineering. Upon graduation in 2014, he began his Masters of Environmental Engineering at NC State under Dr. Andrew Grieshop. He is grateful for all of the experiences that NC State has provided as an undergraduate and graduate student. After graduation, he looks forward to new experiences.

ACKNOWLEDGMENTS

I would like to acknowledge my advisor, Dr. Andrew Grieshop, for providing me with the opportunity to become a successful researcher and for all of his support throughout these years. I would also like to thank Provat Saha, Roshan Wathore, Ryan Repoff, and Aditya Sinha for their help and support in the lab. Finally, I would like to thank the NSF for providing funding for research.

TABLE OF CONTENTS

LIST OF TABLES

LIST OF FIGURES

CHAPTER 1: INTRODUCTION

Approximately 3 billion people in developing countries rely on biomass burning cookstoves for domestic heating and cooking[1]. Incomplete combustion in cookstoves emits a range of pollutants including black carbon (BC), carbon monoxide (CO), particulate matter ($PM_{2.5}$), volatile organic compounds (VOCs), and polycyclic aromatic hydrocarbons (PAHs) linked to a range of adverse health, environmental and climate effects[2–11]. Residential biomass burning contributes ~30% of global emissions of BC, estimated to have the second highest global warming impact after CO_2[3,10,12]. However, the sign and magnitude of net climate effects are uncertain when co-emitted species such as primary organic carbon (OC), the additional uncertain influences of brown carbon (BrC) and the semi-direct and indirect effects are considered[12]. This uncertainty holds for emissions from open (e.g. wildfires and agricultural burning)[13–15] and domestic (cookstove) biomass combustion[16–19]. Efforts to minimize health, climate and other impacts have resulted in the development and dissemination of alternative cookstoves. However, net benefits of alternatives hinge on varying emissions performance[20] and the properties and evolution of emissions[19,21].

Biomass combustion is a continuum encompassing open burning, modern residential wood stoves in developed countries, and small-scale cookstoves in less developed countries (LDCs). Biomass burning as a whole emits roughly 42 and 90% of global BC and primary OC, respectively, with domestic biofuel combustion contributing 30 and 20% of these totals[3]. Combustion conditions vary considerably between modes, influencing the physical and chemical properties of the emissions, even when fuel is held constant. Modified combustion efficiency (MCE; $\Delta CO_2/(\Delta CO+\Delta CO_2)$; where Δ indicates background correction) is a descriptor of combustion completeness often used to delineate smoldering (<0.90) and flaming (>0.90) combustion[22]. Open biomass burning and rudimentary cookstoves result in lower MCEs than more advanced domestic appliances[23]. Combustion conditions and variables including fuel type and moisture content also influence emission parameters such as OC:BC ratio and optical properties[23]. Primary gas- and aerosol emissions from biomass cookstoves have been extensively measured in both field[24,25] and laboratory[26–30] settings. However, research on their physical and chemical characteristics is still limited[29,31–33] and studies of their evolution during atmospheric processing (e.g. to form SOA) are completely lacking.

The quantity, properties and effects of biomass burning emissions evolve during atmospheric oxidation. SOA is formed via condensation of low volatility compounds formed by photo-oxidation of gas-phase species; this formation is typically studied in laboratory studies using smog chambers and/or oxidation flow reactors (OFR). Smog chamber studies allow limited experimental time spans and may be complicated by particle- and vapor-wall-losses[34–39]. OFRs provide an additional method to study SOA formation, by exposing species to oxidant concentrations orders of magnitude greater than in the atmosphere for short residence times (seconds to minutes). Comparisons of laboratory smog chamber and OFR experiments have shown that photo-oxidation of open burning[40,41] and residential woodstove emissions[42–44] can increase OA mass by several-fold with similar evolution in chemical and physical characteristics[44–48]. OA evolution observed in large-scale biomass burning plumes has ranged from significant OA mass enhancement[49–52] to a decreases or no change in mass[53–55], though increases in aerosol oxygenation have been consistently observed[52,53,55,56]. Differences in fuel characteristics, combustion characteristics (e.g. flame temperature) and plume chemical processes likely all contribute to these contrasts. While combustion during open biomass burning and in cookstoves are distinct, burning the same fuel in varying cookstove models may offer insights into how combustion conditions influence the properties of fresh biomass burning emissions and their atmospheric evolution.

To address these needs, this paper describes laboratory aging of emissions from a representative range of biomass cookstove models using a recently developed F-OFR. The specific objectives include to: 1) examine primary emissons of cookstoves operated under several testing protocols; 2) observe SOA formation and the evolution of physical and chemical properties via simulated atmospheric aging; 3) explore the influence of semivolatile vapor losses by exposing whole emissions to oxidants directly after emission and after increasing time in a Teflon chamber; 4) study the influence of stove technology, combustion conditions and oxidant conditions on aerosol properties relevant to climate and regional AQ impacts.

Chapter 2: MATERIALS AND METHOD

2.1 Biomass Cookstoves and Lab Testing Protocols

The three stoves tested span the range of portable biomass cookstoves currently being promoted for use in developing countries (stoves shown in Figure A1). The TSF, an open cooking fire, was the ‘baseline’ technology, with poor combustion efficiency. The intermediate model was a natural-draft ‘rocket’ cookstove (NDS), with an insulated elbow combustion chamber and no chimney, widely distributed in India[29,57,58]. The most advanced model was a forced draft gasifier stove (FDGS) using an electric fan for air injection and improved combustion. The FDGS is one of the cleanest models tested in laboratory settings[26] and has been the basis of several intervention studies[59–61]. Dry red oak (approximately 2x2x15 cm; moisture content<10%) was used as fuel for all tests.

Two laboratory testing protocols were used. First, two phases of the Water Boiling Test (WBT) protocol[62] were used: the ‘cold start’, simulating high-power cooking by rapidly boiling 2.5 L of water, followed by a lower power, 45-minute ‘simmering’ phase. Second, several tests applied a modified testing protocol (MTP) under development to better mimic cooking activity and emissions observed in the field, which often differ substantially from WBT results[24,61,63]. The MTP replicates distributions of normalized $\Delta CO+\Delta CO_2$ observed during field testing[61,64].

2.2 Experimental Setup

Stove tests were conducted in an exhaust hood in which emissions were captured and diluted into a duct (Figure A2 shows experimental schematic). Emission collection lasted from fuel ignition until the end of the testing protocol (~1 to 1.5 hours) during which dilute primary (unaged) emissions were sampled via a probe in the duct. Downstream, a second, heated (120°C) stainless steel probe sampled and additionally diluted emissions by a factor of 2.2 using heated (120°C) dry and filtered compressed air in a stainless steel ejector dilutor (Air-Vac TD110HSS). Thus diluted, emissions were introduced into a clean 8 m^3 Teflon smog chamber[39] to create a 'batched' population of emissions. In parallel, emissions were continuously sampled through the F-OFR (described below); referred to as "online sampling". At the completion of the testing protocol, the F-OFR sampling path was reconfigured to sample emissions from the smog chamber; referred to as "batch sampling".

During online sampling, zero air (Aadco 737 Zero Air Generator) was used to additionally dilute emissions by a factor of two prior to entering the F-OFR to reduce concentration and temperature. The average temperature of dilute emissions inside the sampling duct was 30±0.5°C, while the further diluted emissions exited the F-OFR at 25±0.3°C. Particle concentrations were additionally moderated by a factor of ~1-6 using a partial diversion through a parallel flow path consisting of a diaphragm pump, HEPA filter and mass flow sensor. CO_2 measurements at various points were used as tracers for dilution of emissions. F-OFR bulb setting was constant during online sampling.

During batch sampling, unaged emissions were drawn from the smog chamber (thru a 60°C heated line) to either a bypass line or the F-OFR, alternated with an automated 3-way valve system utilizing a 'dump flow' to maintain constant flow through the F-OFR. No additional dilution was utilized, but the particle line sample was partially filtered as in the online configuration. The unaged batched primary emission population was characterized for ~10 minutes, after which F-OFR aging conditions were varied by adjusting bulb intensity. Primary emissions in the duct were sampled by the Stove Emission Measurement System (STEMS-1G)[61]. In both sampling configurations, gas-phase instruments measured primary emissions downstream of the STEMS and upstream of the F-OFR, and a range of particle- and gas-phase instrumentation measured downstream of the F-OFR, with particle-phase instruments alternating during batch sampling. Particle instruments included: a scanning mobility particle sizer (SMPS) measuring aerosol size distribution (15–685 nm), an aerosol chemical speciation monitor (ACSM) for aerosol composition and mass concentrations[65], a 870 nm photoacoustic extinctiometer (PAX) for particle absorption and scattering, and 3-λ particle soot absorption photometer (PSAP) for multi- wavelength absorption[66] (but not BC concentrations due to loading/scattering filter artifacts[67]). Quartz and Teflon filters were simultaneously collected by the STEMS and downstream of the F-OFR during online sampling for gravimetric and thermo-optical analysis to quantify $PM_{2.5}$ mass and elemental and organic carbon (EC; OC). Section A1 and Table A1 provide details on instrumentation.

Wall losses in the smog chamber and F-OFR were corrected using BC as an inert tracer and assuming internally mixed aerosol[68,69]. To address observed systematic differences between primary OC (from filters) EFs and unaged chamber OA (from ACSM) EFs, corrections for ACSM transmission limitations and for particle wall loss in the smog chamber during loading were applied and are discussed in A2.

2.3 Field-Oxidation Flow Reactor (F-OFR)

A recently constructed F-OFR was used to simulate atmospheric aging of emissions. The F-OFR is a smaller (0.39 m long x 0.15 m diameter; 7 L volume) version of a Potential Aerosol Mass (PAM) reactor[46,70] constructed of thin (0.8 mm) stainless steel to be rugged and portable for future use in rural field campaigns. F-OFR plug-flow residence time was 54-68 seconds at flow rates of 6.1-7.5 L min^{-1}. Particle instruments sampled from the center of the reactor through a copper line and two ozone denuders while gas-phase instruments sampled from a 'ring flow' (a perforated PTFE ring arranged near the outer circumference of the reactor) through PTFE tubing. The F-OFR is constructed of stainless steel to minimize the loss of charged combustion particles and uses two low-pressure mercury lamps (GPH357T5VH/4, Atlantic Ultraviolet) emitting UV light at 185 and 254 nm to produce O_3 and OH radicals[71,72]. The bulbs are housed in Teflon sleeves with a sheath flow to minimize temperature changes and oxidant accumulation near the bulbs. Bulbs intensities were varied using dimmable fluorescent ballasts to vary oxidant concentrations during batch sampling.

Integrated exposure of the sampled air to OH radicals in the reactor was measured using CO (emitted during the combustion process and measured up- and down-stream of the reactor) as a tracer[71,72]. OH exposure in OFRs has been shown to be a function of H_2O mixing ratio, external OH reactivity (OHR) of the sampled air, O_3 concentration, and residence time[71]. A model based on that of Li et al.[71] was developed based on data from CO-only experiments, was used to estimate OH exposure for a single bulb setting, in which the change in the CO tracer was below detection. The model and underlying experiments are discussed in A3 and verify that our reactor performed consistently with other OFR/PAM reactors. The model can be used to estimate OH exposure in cases without an external tracer.

Chapter 3: RESULTS AND DISCUSSIONS

3.1 Influence of Stove Type and Testing Protocol on Primary Emissions

18 total tests (5 TSF; 8 NDS; 4 FDGS) were performed, with 10 and 7 following the WBT and MTP protocols, respectively (Table A2 lists details of all tests). Fuel-based emission factors (EFs; g (kg fuel)$^{-1}$) were calculated using the carbon balance method discussed elsewhere[61], to allow for comparison between experiments and across stove types. Figure 1A shows that across cookstoves and test protocols, $PM_{2.5}$ EF was anti-correlated (R^2=0.68) with MCE. Higher MCE for improved cookstoves indicates more complete combustion; for example, the FDGS tests have the highest (lowest) mean MCE (PM EF). Figure 1A also shows that inter-test variability within an individual stove type is reduced for more efficient stoves. The high variability in TSF tests was likely due to the uncontrolled nature of the combustion. Two-tailed t-tests indicate no significant difference ($P<0.05$) between $PM_{2.5}$ EFs for different testing protocols but significant difference between cookstoves. Because of this overlap, all of the following analysis combines the results from the two testing protocols for a given stove. The lack of significant difference between testing protocols is difficult to explain due to the limited number of experiments and relatively high inter-experiment variability.

Figure 1B shows $PM_{2.5}$, OM, and EC EFs for each cookstove type; OM and EC were the dominant contributors to PM in all tests. The TSF had the highest $PM_{2.5}$ and OM EFs, but lower EC EFs than the alternative cookstoves. Mean NDS and FDGS $PM_{2.5}$/CO (shown in Table A2) EFs were 57%/44% and 74%/58% lower than TSF EFs, respectively. Figure 1B shows the EC and $PM_{2.5}$ EFs of the TSF and NDS were in line with values for similar stoves reported for other laboratory studies, while the FDGS EC and $PM_{2.5}$ EFs were slightly higher than laboratory values[26,28–30] but below those observed during field tests of the same stove[61] (not shown). EC/TC (where TC is total carbon (EC+OC)), ratios for the TSF (0.16±0.07), NDS (0.56±0.13), and FDGS (0.71±0.07) were all greater than the value of 0.1 typical for open biomass burning[56]. Field studies have reported similar EC/TC ranges for TSF (0.15-0.28), rocket/improved (0.30-0.48) and gasifier (0.48-0.70) cookstoves[24,29,61]. This indicates that the improved combustion in alternative stoves (via insulation and targeted air injection) influences the nature of particles emitted under both field and laboratory settings. Therefore, although the NDS and FDGS reduce emissions via improved combustion, the net impact of their emissions may be more climate-warming on a per fuel basis; this will be somewhat offset by reduced fuel use[61]. The reduced EF inter-test variability in more efficient stoves is demonstrated with ±1 σ error bars in Figure 1B. TSF $PM_{2.5}$ EF coefficient of variation (CV) was 0.45 compared to 0.22 and 0.38 for the NDS and FDGS cookstoves, respectively. This represents inter-test variability and indicates the difficulty of comparing results between individual tests due to potential influence of user activity and variation in fuels, even for a specific fuel type. To address this variability, results will be presented as stove averages along with individual test data for subsequent analysis.

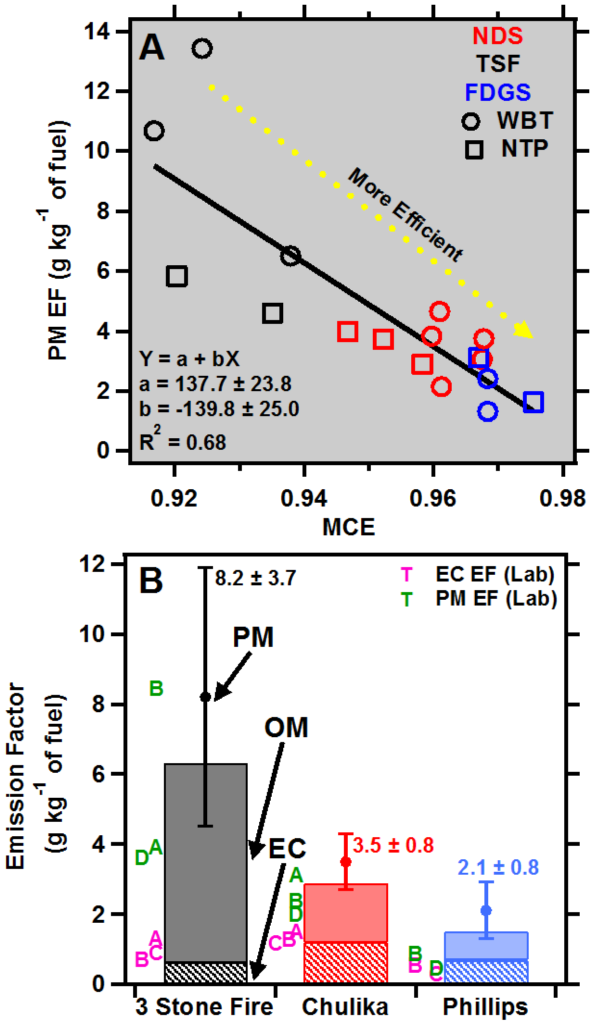

Figure 1. Influence of stove technology and testing protocols on unaged emission factors from filter-based analyses. (a) $PM_{2.5}$ EF for the WBT and MTP across a range of MCE values averaged over the burn duration. Solid black line is a linear regression fit (b) Average primary $PM_{2.5}$, OM, and EC EFs for each cookstove model. Error bars for the $PM_{2.5}$ EFs represent ± 1 σ among all experiments for both testing protocols. Primary OC (from filters) EFs were used to determine primary organic matter (OM) EFs based on OM:OC ratios estimated on a per-test basis using the Improved-Ambient method[73–75] based on unaged f_{44} measured during batch bypass sampling. OM:OC values are reported in Table A2. OC and EC EFs were determined from thermo-optical OC/EC analysis. Laboratory experiments from literature are shown for each cookstove type with letters: (A:Preble et al., B:Just et al., C:MacCarty et al., D: Jetter et al.)[26,28–30]; horizontal position of letters is shifted only for readability.

Figure 2 explores the variation in the chemical composition of POA across stove technology and testing protocol. Figure 2A and 2B shows the trend of f_{44} (a marker for oxygenated species, largely from the CO_2^+ ion fragment)[76,77] and f_{60} (a fragment associated with levoglucosan, often used as a common tracer for biomass burning POA)[78,79] in ACSM spectra against the test-average MCE. Significant differences ($P<0.05$) in f_{44} and f_{60} between cookstove models were observed, but not between testing protocols. f_{44} (f_{60}) consistently increases (decreases) with increasing MCE. This indicates that OA emitted by improved cookstoves contains a greater initial fraction of oxygenated organic species and a reduced contribution from primary markers for biomass combustion, even for the same fuel. The highly oxygenated POA ($f_{44}>25\%$) observed for the FDGS emissions is similar to values reported for modern log burners[80,81] and may be associated with higher aerosol mass-specific mutagenicity for these emissions[31]. The f_{44}/f_{60} values reported for the TSF are within the range ($f_{44}<10\%$; $f_{60}>2.5\%$) observed in laboratory-simulated open burns[41,43] and ambient measurements[79]. f_{44} and f_{60} have been shown to be a function of combustion phase with some studies reporting elevated f_{44} values in smoldering[43,82,83] phase and others in the flaming phase[84] emissions. Figure 2 report our results alongside those from smoldering (pink points) and flaming (purple points) phase emissions from a modern wood burning stove burning different fuels[82]. The reported f_{44} and f_{60} values for Oak are within our range for the TSF and NDS, suggesting that similar dynamics are occurring in the combustion zone for a modern heating stove and natural draft cookstoves[82]. Our results characterize an emission population from a full burn, encompassing high- and low-power operation, and are within the range of values reported for these modern heating stove emissions.

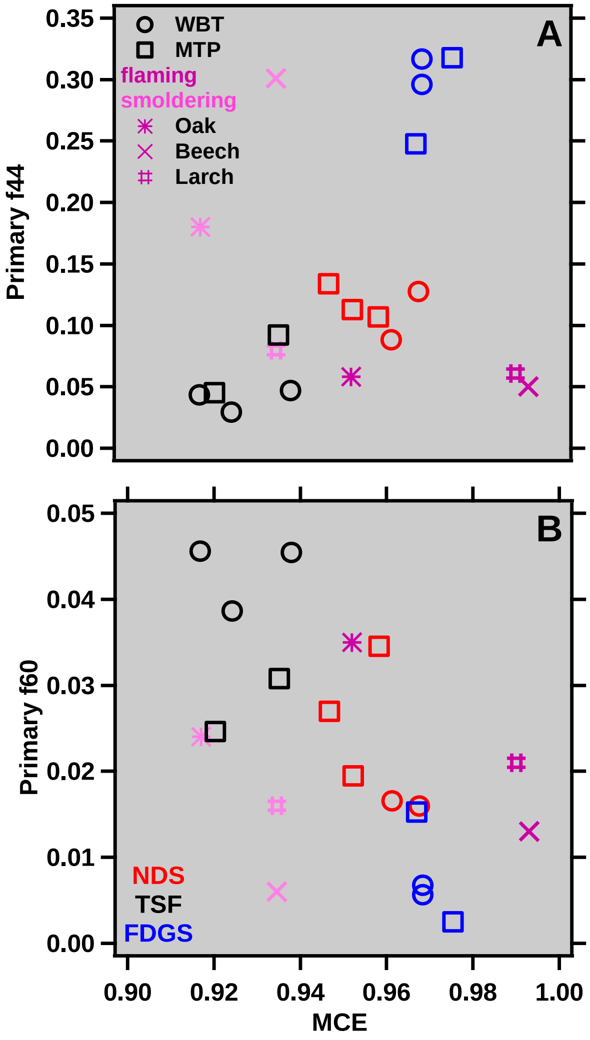

Figure 2. POA organic aerosol composition as indicated by ACSM fragment contributions across testing protocols and stove technology. Fractional contribution of organic aerosol tracer fragments versus full-test MCE for (a) oxidized species (f_{44}), and (b) biomass burning tracer (f_{60}). Purple data points are different fuels (Oak, Beech, Larch) combusted in a modern wood burner during the smoldering (pink points) and flaming phase (purple points)[82]. MCE is the average for the burn duration and f_{44} and f_{60} markers represent a full burn emission population characterized by bypass scans during batch sampling from smog chamber.

3.2 Secondary Organic Aerosol Formation Potential of Cookstove Emissions

SOA production during batch sampling was quantified using the OA enhancement ratio (OA ER)[42]. Absolute OA enhancement was determined by the difference in aged OA (F-OFR sampling) and fresh OA (bypass sampling), as shown in Figure A3. OA ER was defined as the total detected mass ($POA_{batch(t=0)}$ + absolute enhancement) normalized by $POA_{batch(t=0)}$, where $POA_{batch(t=0)}$ is the initial loading in the chamber at the end of the burn duration corrected for ACSM particle size detection window limitations and wall loss during the injection period (Section A2). OA ER values >1 indicate a net increase in OA mass. A linear regression of POA EFs collected on filters and corrected chamber POA EFs measured by the ACSM (slope=0.84±0.10, R^2=0.87) is shown in Figure A4. The slope of 0.84 is a reasonable comparison considering uncertainties from various sources: filter artifact corrections, parameterized OM:OC ratios, ACSM particle size detection limitations, and chamber particle wall loss during loading. Figure 3A shows OA enhancement observed for all stoves during batch sampling across a range of aging conditions. A net increase in mass is indicative of SOA formation by gas-phase and/or heterogeneous oxidation processes; we cannot distinguish the two processes during F-OFR oxidation of whole emissions. With further aging, processes such as evaporation (e.g. due to the dominance of fragmentation reactions[48]) may drive a reduction in mass. A net increase in OA mass was observed for all conditions with bulbs on, indicating substantial SOA production under all aging conditions. Average OA ER ranged between 1.17±0.01 and 3.02±0.51 for integrated OH exposures between 1.8e11 and 6.5e11 molecules s cm^{-3}. This range of OH exposures is equivalent to 1.4±0.3 to 5.1±0.6 days assuming a daily-average OH concentration of 1.5e6 molecules cm^{-3}. The TSF showed the greatest OA mass enhancement with a maximum aged OA concentration of three times the initial POA mass after 1.4±0.3 days of equivalent aging and a subsequent decrease with additional exposure. Our results are broadly consistent with those of other studies who have measured OA enhancement in emissions from other forms of biomass combustion[40–44,81,85]. Combustion device clearly influences mass enhancement[42–44,81,85] but fuel type appears to have a greater effect on how emissions evolve with aging[40,41]. The observed decrease in OA ERs with further aging, not seen in other aging experiments[48], is likely due our higher peak OH exposures.

Our results demonstrate the range of potential SOA formation associated with emissions from commercially available cookstove technologies. Figure 3B shows unaged POA and EC EFs and represents OA production during F-OFR aging as an SOA EF, conceptually similar to primary EFs. The peak SOA EF for each cookstove occurred between 2.8 to 5.4 days of aging before decreasing with continued exposure. This suggests that SOA-forming potential and time of peak enhancement of emissions is dependent on cookstove technology. An implication of neglecting this SOA production is that potential $PM_{2.5}$ impacts may be underestimated by a factor of 2 to 3. TSF tests showed the highest and most variable SOA EF; these were substantially less for more efficient cookstoves. The CV of SOA EF for repeated experiments of the TSF (0.57), NDS (0.51), and FDGS (0.17) indicate that variability declines with increasing combustion efficiency. This variability is likely driven by the ability to control the combustion process in repeated experiments with the same cookstove, but may also be due to precursor emissions that change due to process/fuel variability[85].

A recent modeling study suggested that SOA formation from biomass burning emissions could be limited in smog chambers by the up to 40% of primary semi-volatile vapors loss to chamber walls occurring within hours. However, another study has suggested that SOA production is dominated (~80% of observed SOA) by higher volatility compounds[37,86] less apt to partition to chamber walls. Two lines of evidence from our tests suggest that vapor losses in our system did not have a major influence on observed SOA production. First, consistent OA enhancements were observed at equivalent OH exposures over time during batch-mode OFR aging, despite sharply decreasing POA concentrations (Figure A5A-C). Figure A5 explores the OA enhancement in the chamber over time. During each experiment, a sequence of four bulb settings was used and then cycled in reverse order in a second pass. Second, the total aged OA EFs (POA+SOA) measured during online and batch configurations (during and after the burn) are in reasonable agreement (Figure A5D). Online aged OA EFs were slightly higher (average of 50%) than those from batch measurements, which could be explained by losses of precursors at very early stages in the experiment. However, numerous factors contribute to uncertainty in this comparison. For example, the various loss corrections (Sec. A2) and the calculation of an average OH exposure may not apply equally to 'steady state' batch and highly time-varying online measurements. Therefore, while our results suggest a negligible role for vapor losses on a longer (multi-hour) time frame, we cannot eliminate the possibility that precursors are lost during the initial injection period.

Figure 3. Exploring the evolution of OA ER and SOA EF across range of atmospheric aging conditions and cookstove technologies. (A) OA enhancement as a function of OH exposure shown for all exposure conditions/tests (faded points) and averaged by approximately 2 days of equivalent binned OH exposures ± 1 σ (dark points) for each cookstove model. (B) Averaged POA, EC, and SOA EF ± 1 σ are shown for each stove for fresh emissions (left bar) and after aging in batch configuration at peak SOA enhancement (middle bar) and peak OH exposure (right bar) with numbers indicating equivalent days of aging. Fresh EFs are based on thermo-optical OC/EC analysis (OC converted to OM using Improved-Ambient derived OM:OC ratios) of unaged filters. POA and EC EFs reported for 'aged' bars are based on chamber loadings and corrected for ACSM transmission window and particle losses during chamber loading to allow for representative comparison to BC measurements and integrated filter samples. Batch sampling EC EFs are based on PAX absorption measurements using a MAC of 3.33 ± 0.21 (m^2 g^{-1}) shown in Figure A7. SOA EFs at the peak enhancement and exposure are based on the absolute OA enhancement normalized to mass of wood burned using the carbon balance method.

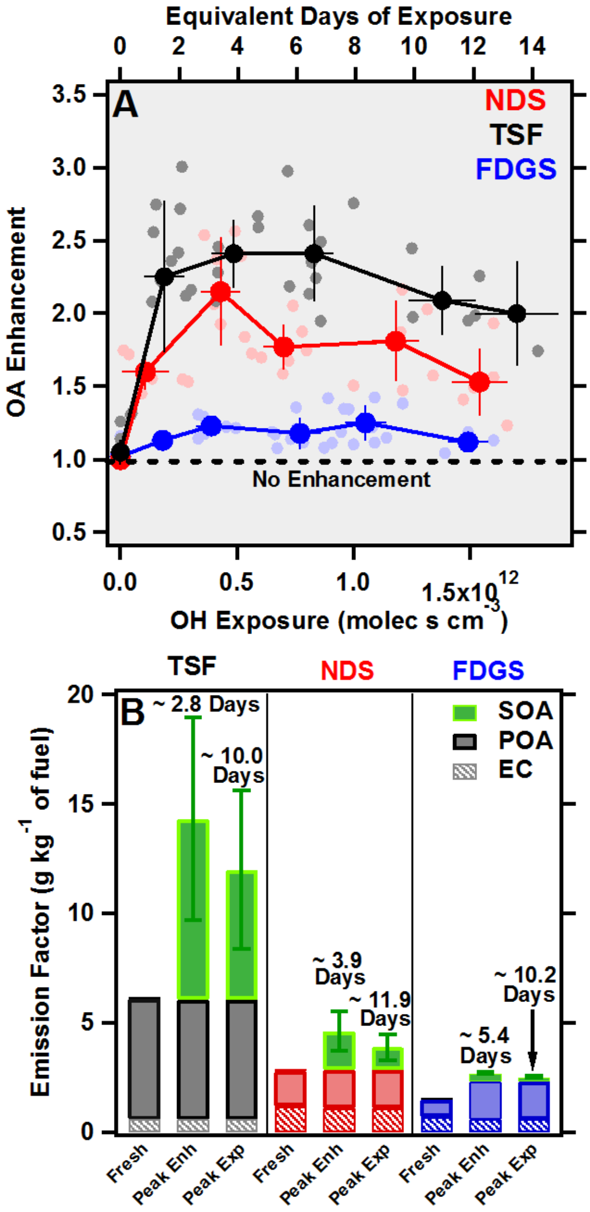
Equivalent Days of Exposure
0
2
4
6
8
10
12
14
A
NDS
TSF
FDGS
OA Enhancement
3.5
3.0
2.5
2.0
1.5
1.0
0.5
No Enhancement
0.0
0.5
1.0
1.5x10^12
OH Exposure (molec s cm^-3)
TSF
NDS
FDGS
B
~ 2.8 Days
~ 10.0 Days
~ 3.9 Days
~ 11.9 Days
~ 5.4 Days
~ 10.2 Days
SOA
POA
EC
Emission Factor (g kg^-1 of fuel)
20
15
10
5
0
Fresh
Peak Enh
Peak Exp
Fresh
Peak Enh
Peak Exp
Fresh
Peak Enh
Peak Exp

3.3 Evolution of Cookstove OA Chemical Composition during Photo-oxidation

ACSM mass spectra of unaged and aged OA provide insight into the chemical evolution of cookstove emissions during OFR processing. Changes in f44, f43, and f60 (fractional contribution to OA spectra from *m/z* 44, 43 and 60, respectively) shown in Figure 4A demonstrate the evolution of chemical composition with increased OH exposure during batch aging experiments. In most cases, OH exposure increases f44 and decreases f43 and f60, suggesting that more oxidized components dominate the aged emissions and that levoglucosan or other species contributing at m/z 60 are rapidly oxidized[87]. The f44 for FDGS POA is initially very high and this and other fragments evolve relatively little with additional aging, consistent with the small observed OA enhancement. Ortega et al. aged open-burning emissions from varied fuel types and observed an increasing rate of f44 enhancement for POA with greater initial f44[41]. We did not observe this trend across cookstove emissions with a single fuel, highlighting the important influence of varying combustion conditions on OA (Figure A8). There is some evidence of OA contribution at *m/z* 28 (CO^+) in our tests as in other biomass burning spectra[41,88] (Sec. A4), but ACSM signal-to-noise was insufficient to reliably quantify this, and so the default fragmentation table, in which this organic fragment is neglected, was applied.

To extend the evaluation of OA composition, atomic ratios (H:C; O:C) were estimated using the 'Improved-Ambient' parameterization using f43 and f44 described in detail in section A5[73–75]. The results of this analysis are shown in Figure 4B using a Van Krevelen diagram[89]. Elemental ratios provide insight into the processes driving the oxidation reactions in these complex and highly variable systems. During batch sampling, OA ERs increased and then decreased with progressively greater OH exposure. However, O:C ratios continually increased with more exposure (even with mass decreases) indicating a possible dominance of fragmentation reactions[48]. Figure 4B also shows that unaged emissions' H:C (O:C) ratios consistently decrease (increase) as combustion efficiency improves. The slope in Van Krevelen space for POA from different combustion types was -0.20±0.01, while that for increasing F-OFR oxidation was between -0.09±0.03 and -0.13±0.05, depending upon cookstove type. These slopes reflect the functionalization and fragmentation pathways occurring during combustion and aging processes[41]. Slopes between -1.0 and -0.5 typically indicate the addition of both an acid (COOH) and alcohol (OH) functional group or the addition of just an acid group via fragmentation of C-C bonds[90].

Regression fit lines in Figure 4B show that relatively similar trends were observed across varying combustion efficiencies (dashed line) and as emissions from different cookstoves are photo-chemically aged (solid lines). This suggests that similar OA functionalization pathways are occurring during combustion and atmospheric processes, but on very different timescales. This also suggests that combustion conditions (even within flaming combustion), and not only fuel, play a major role in differences in OA emissions and properties between plume and lab-scale burning. Emissions aged through the F-OFR during online sampling (open circles) had H:C and O:C ratios consistent to those at equivalent batch OH exposures, indicating that similar chemical processes are driving SOA formation during both online and batch sampling. Results presented by Ortega et al. of lab-simulated open biomass burning emissions from a range of unprocessed fuels aged in a PAM reactor resulted in distinct slopes of primary (-0.87±0.01) and aged emissions (-0.70±0.01)[36]. The difference in slopes between this study and ours may be due to differences between open biomass combustion and controlled combustion, or simply that we only used one fuel type. Different fuels resulted in unique slopes (-0.50±0.02 for turkey oak;

0.02±0.03 for ponderosa) indicating that fuel type influences oxidation processes[41]. This difference was attributed to the emission of acids during combustion of softwoods (i.e. spruce) that are not found in hardwoods (i.e. oak)[81]. The observed slope from our unaged and aged emissions are comparable to oxidized emissions from a heavily loaded residential wood burner using beech fuel (0.19±0.05), despite lower initial H:C ratios[85]. A combination of variables such as fuel type and combustion conditions influences the evolution of biomass burning emissions[41,81,82,85].

Figure 4C extends the van Krevelen plot typically used to visualize the evolution of atmospheric OA[89] to show O:C and H:C ratios including contributions from aerosol refractory carbon, which plays an important and varying role in emissions from different stoves (A6 describes the calculation). Also shown on this panel are points/regions indicating the location of wood components (lignin, cellulose)[91], end-points of incomplete biomass combustion (char, soot) and oak in raw, pyrolyzed and combusted forms[92]. The figure shows that emissions from the TSF are more similar to lignin than char or soot and fall between the raw and combusted/pyrolyzed oak, consistent with the large contribution of soot and less-oxygenated volatiles to the emitted aerosol. As combustion efficiency improves, H:C ratios decrease, presumably due to the enhanced role of dehydration and demethylation in the evolution of the fuelwood[91,93,94]. Primary aerosol emissions from the NDS and FDGS fall near the char region, consistent with the much greater EC/TC ratios and relatively small contributions from OA (Figures 1, 5). Fresh FDGS emissions appear to have substantially higher O:C ratios than those from other stoves possibly due to dominant contributions from high temperature carboxylation or oxidation reactions[93]. However, after oxidation in the F-OFR, O:C of the NDS and TSF emissions increase to roughly the same end-point as the FDGS, which shows relatively little change during oxidation. Estimated H:C for all emissions slightly increase during oxidation. The overall trend is consistent with the possible role of both oxidation and hydration reactions during aging of aerosols[91]. Further chemical characterization of emissions may provide more generalizable insights about the evolution of products during varied combustion and oxidation conditions.

Figure 4. Variation in ACSM OA fragment contributions and estimated elemental composition with stove and photochemical aging. Averaged±1 σ unaged (cross symbol) and aged (large circle) values across all tests for each stove type are shown. Unaged (small faded circle) and aged (small circle, colored by OH exposure) values per test are also shown. Aged measurements during the online configuration are shown with an open circle. (a) organic aerosol fragments f44 vs f43, and (B) f60 (C) estimated H:C and O:C ratios averaged by binned (~2 days) OH exposure. Solid lines are linear regression lines for each stove type; slopes represent functionalization pathways[89]. Dashed line indicates the slope of unaged H:C and O:C ratios across stove types. Data from aged open biomass burning of Turkey Oak from Flame-3 are shown with green circles[41]. The dotted cyan line indicates the upper bond of the region typically observed during ambient measurements[35]. (D) H:C and O:C ratios including refractory black carbon averaged by binned (~2 days) OH exposures. Shaded regions represent typical values for Soot, char[92], lignin, and cellulose[91].

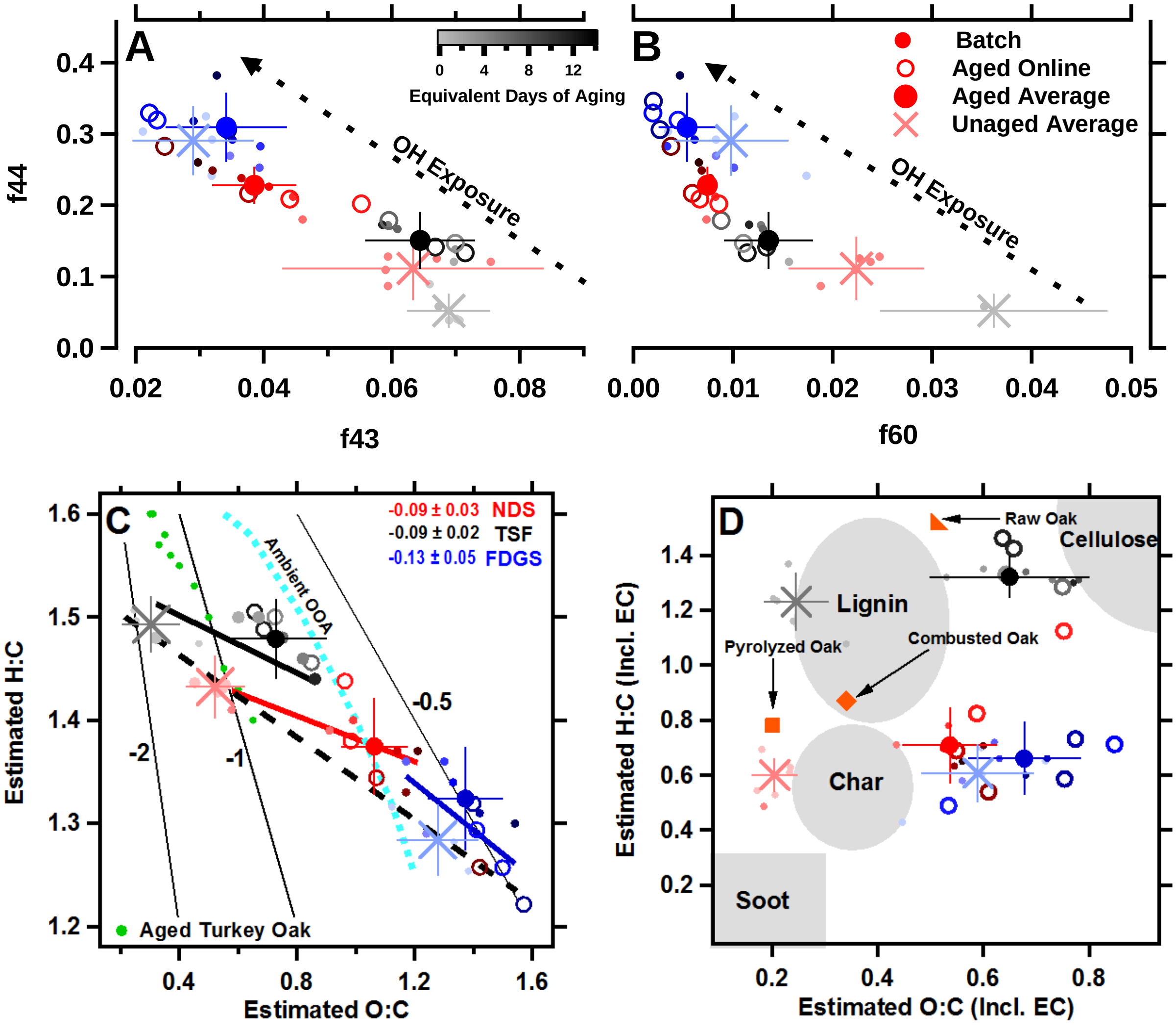
A
B
f44
0.0
0.1
0.2
0.3
0.4
0.02
0.04
0.06
0.08
f43
0.00
0.01
0.02
0.03
0.04
0.05
f60
0
4
8
12
Equivalent Days of Aging
OH Exposure
OH Exposure
Batch
Aged Online
Aged Average
Unaged Average
C
Estimated H:C
Estimated O:C
1.2
1.3
1.4
1.5
1.6
0.4
0.8
1.2
1.6
-0.09 ± 0.03 NDS
-0.09 ± 0.02 TSF
-0.13 ± 0.05 FDGS
Ambient OOA
-0.5
-1
-2
Aged Turkey Oak
D
Estimated H:C (Incl. EC)
Estimated O:C (Incl. EC)
0.2
0.4
0.6
0.8
1.0
1.2
1.4
Raw Oak
Cellulose
Lignin
Pyrolyzed Oak
Combusted Oak
Char
Soot

3.4 Effect of Combustion Conditions and Aging on Particle Optical Properties

Cookstove combustion and atmospheric evolution directly affect OA/BC ratio of aerosols, which is linked to optical properties with important climate forcing implications. Figure 5A displays the average unaged and aged peak OA/BC ratio for each cookstove type. The OA/BC ratio for alternative cookstoves is much lower, indicating that net direct specific warming from aerosols from alternative cookstoves is greater than those from the TSF. This observed difference in OA/BC ratio is possibly due to the combustion temperature in different stove models. For example, low-temperature smoldering emissions have been shown to produce much greater OA/BC ratios than the flaming phase due to the absence of BC formation[95]. The single scattering albedo (measured at λ=870 nm) also decreased with increasing MCE and as EC compromises a greater fraction of the TC (Section A8, Figure A9). The difference in OA/BC ratio between the TSF and the alternative cookstoves becomes more pronounced after aging. After aging the TSF OA/BC ratio exceeds 10, a threshold sometimes used to indicating a negative net direct radiative forcing[96]. The lower OA/BC ratio for the alternative cookstoves compared to the TSF before and after aging suggests limited aerosol radiative forcing benefits from introduction of alternative cookstoves.

The Absorption Angstrom exponent (AAE) describes the wavelength dependence of aerosol light absorption, using the equation ($b_{abs}=\alpha\lambda^{-AAE}$) with pure BC having an AAE of 1 across all wavelengths[97–99]. Values of AAE greater than 1 suggest the presence of BrC, OA that absorbs light at shorter wavelengths[66,95,100,101]. The difference between the measured absorption at a wavelength and the expected contribution from black carbon is called the BrC fraction of total absorption[102]. Figure 5B presents the stove-average aged and unaged AAE (±1 σ). The values of

AAE for the TSF, NDS, and FDGS are 1.67±0.24, 1.36±0.06, and 1.30±0.05. These are at the lower end of the range of 1.35 to 2.15 reported for open burning emissions[66]. Although Saleh et al. observed a slight enhancement of AAE with photochemical aging in a smog chamber[66], other studies have reported no change or a decrease with photochemical aging[95,100]. AAE enhancement may be a function of the extent of aging, which was relatively minimal in the study of Saleh et al.[66]. Figure 5B shows that AAEs measured in our study did not increase and in some cases decreased with aging, possibly due to photo-bleaching of BrC[103]. Figure 5C suggests that while all cookstove emissions have a non-trivial BrC contribution to absorption (~10-35%) at each PSAP wavelength (470, 522, and 660nm), there is substantially less BrC contribution in alternative cookstove emissions.

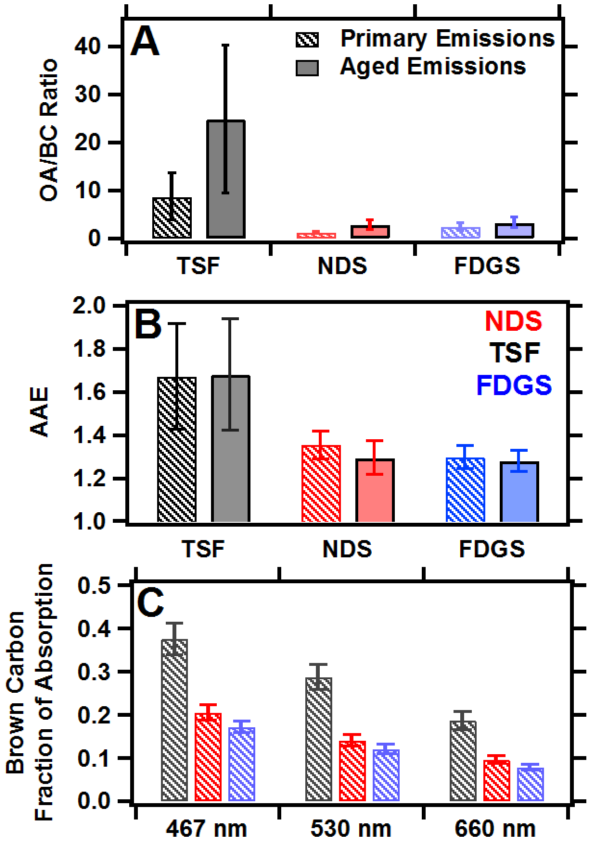

Figure 5. Influence of stove model and aging on optical properties of emitted aerosol. (a) Unaged OA/BC ratios compared to the peak OA/BC ratio after aging during batch sampling for each cookstove (b) Unaged and aged AAE based on the slope of a power law fit of absorption measurements across PSAP wavelengths (467, 530, 660) and interpolated to 870nm (c) BrC fraction of absorption in unaged emissions, determined by the difference between the measured absorption and the expected absorption from BC (AAE = 1) across all wavelengths.

Chapter 4: IMPLICATIONS AND EXTENSIONS

Although improved cookstoves reduce fuel use and emissions of both primary and secondary aerosol species, our results emphasize that benefits from a climate mitigation standpoint are less clear. Primary traditional stove (TSF) emissions had much greater OA/BC ratios, associated with less warming or even cooling, than alternative cookstoves. This difference is enhanced with aging due to greater formation of (not apparently light-absorbing) SOA for the TSF than for alternative stoves. Therefore, aging appears to makes aerosol climate forcing reductions from alternative biomass stoves less likely. However, the benefits from alternative cookstoves adoption air pollution may be substantially greater than suggested by only comparing primary emissions. SOA production from cookstove emissions should be incorporated into air quality models and climate models to represent their evolution in the days to weeks after being emitted.

Our measurements of primary and aged emissions emphasize that the properties of emissions from different stoves vary dramatically. For example, the highly oxygenated OA from the FDGS is distinct from that typically measured for biomass burning emissions and showed relatively minimal evolution during aging. FDGS emissions had the highest specific mutagenicity[30] in lab experiments and were associated with no reduction in childhood pneumonia in a field trial.[56] These outcomes could be associated with the stove's emissions of smaller, highly oxygenated particles. Further, field performance of cookstoves is often far worse than in lab conditions.[23,58] Additional measurements of primary and aged emissions should be conducted under real-world conditions to better understand potential health and climate benefits of these stoves.

The OA enhancements due to aging observed in our study are consistent with those for emissions from similar fuels during open burning and use in modern heating stoves collected with a variety of methods (OFRs; smog chambers). Therefore, the magnitude of enhancement and variation with stove type/efficiency are likely well-represented through our OFR experiments. However, recent work has revealed several issues to be considered when interpreting results of OFR analysis[70,101]. For example, various pathways (other than formation of new OA mass) available to condensable vapors formed during oxidation (e.g. loss to reactor walls) may affect observed OA enhancement[101]. Analysis presented in Section A8, Figure A10 indicates that, due to the high particle number concentrations in our experiments, this was not a major concern. Another concern for OFR experiments is the representativeness of oxidation in the reactor for atmospheric conditions. Recent analysis suggests that our operation of the OFR (as in many past studies) means that chemistry in our reactor was likely less-representative of atmospheric oxidation than is ideal, A10B[70]. For example, UV photolysis of some species likely plays a larger relative role than in real atmospheric oxidation, due to the suppression of OH at low RH/high OHR. Therefore, future work will modify operating conditions to assess the influence of OFR conditions on aging of emissions.

REFERENCES

(1) Foell, W.; Pachauri, S.; Spreng, D.; Zerriffi, H. Household cooking fuels and technologies in developing economies. *Energy Policy* **2011**, *39* (12), 7487–7496.

(2) Shen, G.; Wang, W.; Yang, Y.; Ding, J.; Xue, M.; Min, Y.; Zhu, C.; Shen, H.; Li, W.; Wang, B.; et al. Emissions of PAHs from Indoor Crop Residue Burning in a Typical Rural Stove: Emission Factors, Size Distributions, and Gas−Particle Partitioning. *Environ. Sci. Technol.* **2011**, *45* (4), 1206–1212.

(3) Bond, T. C. A technology-based global inventory of black and organic carbon emissions from combustion. *J. Geophys. Res.* **2004**, *109* (D14).

(4) Naeher, L. P.; Brauer, M.; Lipsett, M.; Zelikoff, J. T.; Simpson, C. D.; Koenig, J. Q.; Smith, K. R. Woodsmoke Health Effects: A Review. *Inhal. Toxicol.* **2007**, *19* (1), 67–106.

(5) Lim, S.; Flaxman, A.; Danaei, G.; Shibuya, K.; Adair-Rohani, H.; ALMazroa, M.; Amann, M.; Anderson, H.; Andrews, K.; Aryee, M.; et al. A comparative risk assessment of burden of disease and injury attributable to 67 risk factors and risk factor clusters in 21 regions, 1990–2010: a systematic analysis for the Global Burden of Disease Study 2010 http://www.sciencedirect.com/science/article/pii/S0140673612617668 (accessed Nov 18, 2015).

(6) Pope, D. P.; Mishra, V.; Thompson, L.; Siddiqui, A. R.; Rehfuess, E. A.; Weber, M.; Bruce, N. G. Risk of Low Birth Weight and Stillbirth Associated With Indoor Air Pollution From Solid Fuel Use in Developing Countries. *Epidemiol. Rev.* **2010**, *32* (1), 70–81.

(7) Chafe, Z. A.; Brauer, M.; Klimont, Z.; Van Dingenen, R.; Mehta, S.; Rao, S.; Riahi, K.; Dentener, F.; Smith, K. R. Household Cooking with Solid Fuels Contributes to Ambient PM2.5 Air Pollution and the Burden of Disease. *Environ. Health Perspect.* **2014**.

(8) Menon, S. Climate Effects of Black Carbon Aerosols in China and India. *Science* **2002**, *297* (5590), 2250–2253.

(9) Hansen, J.; Nazarenko, L. Soot climate forcing via snow and ice albedos. *Proc. Natl. Acad. Sci.* **2004**, *101* (2), 423–428.

(10) Ramanathan, V.; Carmichael, G. Global and regional climate changes due to black carbon. *Nat. Geosci.* **2008**, *1* (4), 221–227.

(11) Rosenthal, J. The Real Challenge for Cookstoves and Health: More Evidence. *EcoHealth* **2015**, *12* (1), 8–11.

(12) Bond, T. C.; Doherty, S. J.; Fahey, D. W.; Forster, P. M.; Berntsen, T.; DeAngelo, B. J.; Flanner, M. G.; Ghan, S.; Kärcher, B.; Koch, D.; et al. Bounding the role of black carbon

in the climate system: A scientific assessment: BLACK CARBON IN THE CLIMATE SYSTEM. *J. Geophys. Res. Atmospheres* **2013**, *118* (11), 5380–5552.

(13) Chung, C. E.; Ramanathan, V.; Decremer, D. Observationally constrained estimates of carbonaceous aerosol radiative forcing. *Proc. Natl. Acad. Sci.* **2012**, *109* (29), 11624–11629.

(14) Jacobson, M. Z. Global direct radiative forcing due to multicomponent anthropogenic and natural aerosols. *J. Geophys. Res. Atmospheres* **2001**, *106* (D2), 1551–1568.

(15) Jacobson, M. Z. Effects of biomass burning on climate, accounting for heat and moisture fluxes, black and brown carbon, and cloud absorption effects: Effects of biomass burning on climate. *J. Geophys. Res. Atmospheres* **2014**, *119* (14), 8980–9002.

(16) Bond, T. C.; Bhardwaj, E.; Dong, R.; Jogani, R.; Jung, S.; Roden, C.; Streets, D. G.; Trautmann, N. M. Historical emissions of black and organic carbon aerosol from energy-related combustion, 1850-2000: HISTORICAL BC/OC EMISSIONS. *Glob. Biogeochem. Cycles* **2007**, *21* (2), n/a-n/a.

(17) Koch, D.; Bond, T. C.; Streets, D.; Unger, N.; van der Werf, G. R. Global impacts of aerosols from particular source regions and sectors. *J. Geophys. Res.* **2007**, *112* (D2).

(18) Lacey, F.; Henze, D. Global climate impacts of country-level primary carbonaceous aerosol from solid-fuel cookstove emissions. *Environ. Res. Lett.* **2015**, *10* (11), 114003.

(19) Kodros, J. K.; Scott, C. E.; Farina, S. C.; Lee, Y. H.; L'Orange, C.; Volckens, J.; Pierce, J. R. Uncertainties in global aerosols and climate effects due to biofuel emissions. *Atmospheric Chem. Phys.* **2015**, *15* (15), 8577–8596.

(20) Grieshop, A. P.; Marshall, J. D.; Kandlikar, M. Health and climate benefits of cookstove replacement options. *Energy Policy* **2011**, *39* (12), 7530–7542.

(21) Lacey, F. G.; Henze, D. K.; Lee, C. J.; van Donkelaar, A.; Martin, R. V. Transient climate and ambient health impacts due to national solid fuel cookstove emissions. *Proc. Natl. Acad. Sci.* **2017**, *114* (6), 1269–1274.

(22) Collier, S.; Zhou, S.; Onasch, T. B.; Jaffe, D. A.; Kleinman, L.; Sedlacek, A. J.; Briggs, N. L.; Hee, J.; Fortner, E.; Shilling, J. E.; et al. Regional Influence of Aerosol Emissions from Wildfires Driven by Combustion Efficiency: Insights from the BBOP Campaign. *Environ. Sci. Technol.* **2016**, *50* (16), 8613–8622.

(23) Andreae, M. O.; Merlet, P. Emission of trace gases and aerosols from biomass burning. *Glob. Biogeochem. Cycles* **2001**, *15* (4), 955–966.

(24) Roden, C. A.; Bond, T. C.; Conway, S.; Osorto Pinel, A. B.; MacCarty, N.; Still, D. Laboratory and field investigations of particulate and carbon monoxide emissions from traditional and improved cookstoves. *Atmos. Environ.* **2009**, *43* (6), 1170–1181.

(25) Kar, A.; Rehman, I. H.; Burney, J.; Puppala, S. P.; Suresh, R.; Singh, L.; Singh, V. K.; Ahmed, T.; Ramanathan, N.; Ramanathan, V. Real-Time Assessment of Black Carbon Pollution in Indian Households Due to Traditional and Improved Biomass Cookstoves. *Environ. Sci. Technol.* **2012**, *46* (5), 2993–3000.

(26) MacCarty, N.; Ogle, D.; Still, D.; Bond, T.; Roden, C. A laboratory comparison of the global warming impact of five major types of biomass cooking stoves. *Energy Sustain. Dev.* **2008**, *12* (2), 56–65.

(27) Jetter, J. J.; Kariher, P. Solid-fuel household cook stoves: Characterization of performance and emissions. *Biomass Bioenergy* **2009**, *33* (2), 294–305.

(28) Jetter, J.; Zhao, Y.; Smith, K. R.; Khan, B.; Yelverton, T.; DeCarlo, P.; Hays, M. D. Pollutant Emissions and Energy Efficiency under Controlled Conditions for Household Biomass Cookstoves and Implications for Metrics Useful in Setting International Test Standards. *Environ. Sci. Technol.* **2012**, *46* (19), 10827–10834.

(29) Just, B.; Rogak, S.; Kandlikar, M. Characterization of Ultrafine Particulate Matter from Traditional and Improved Biomass Cookstoves. *Environ. Sci. Technol.* **2013**, 130319140434009.

(30) Preble, C. V.; Hadley, O. L.; Gadgil, A. J.; Kirchstetter, T. W. Emissions and Climate-Relevant Optical Properties of Pollutants Emitted from a Three-Stone Fire and the Berkeley-Darfur Stove Tested under Laboratory Conditions. *Environ. Sci. Technol.* **2014**, *48* (11), 6484–6491.

(31) Mutlu, E.; Warren, S. H.; Ebersviller, S. M.; Kooter, I. M.; Schmid, J. E.; Dye, J. A.; Linak, W. P.; Gilmour, M. I.; Jetter, J. J.; Higuchi, M.; et al. Mutagenicity and Pollutant Emission Factors of Solid-Fuel Cookstoves: Comparison with Other Combustion Sources. *Environ. Health Perspect.* **2016**, *124* (7).

(32) Stockwell, C. E.; Yokelson, R. J.; Kreidenweis, S. M.; Robinson, A. L.; DeMott, P. J.; Sullivan, R. C.; Reardon, J.; Ryan, K. C.; Griffith, D. W. T.; Stevens, L. Trace gas emissions from combustion of peat, crop residue, domestic biofuels, grasses, and other fuels: configuration and Fourier transform infrared (FTIR) component of the fourth Fire Lab at Missoula Experiment (FLAME-4). *Atmospheric Chem. Phys.* **2014**, *14* (18), 9727–9754.

(33) Stockwell, C. E.; Veres, P. R.; Williams, J.; Yokelson, R. J. Characterization of biomass burning smoke from cooking fires, peat, crop residue and other fuels with high resolution proton-transfer-reaction time-of-flight mass spectrometry. *Atmospheric Chem. Phys. Discuss.* **2014**, *14* (15), 22163–22216.

(34) Matsunaga, A.; Ziemann ‡, P. J. Gas-Wall Partitioning of Organic Compounds in a Teflon Film Chamber and Potential Effects on Reaction Product and Aerosol Yield Measurements. *Aerosol Sci. Technol.* **2010**, *44* (10), 881–892.

(35) Ng, N. L.; Canagaratna, M. R.; Zhang, Q.; Jimenez, J. L.; Tian, J.; Ulbrich, I. M.; Kroll, J. H.; Docherty, K. S.; Chhabra, P. S.; Bahreini, R.; et al. Organic aerosol components observed in Northern Hemispheric datasets from Aerosol Mass Spectrometry. *Atmospheric Chem. Phys.* **2010**, *10* (10), 4625–4641.

(36) Zhang, X.; Cappa, C. D.; Jathar, S. H.; McVay, R. C.; Ensberg, J. J.; Kleeman, M. J.; Seinfeld, J. H. Influence of vapor wall loss in laboratory chambers on yields of secondary organic aerosol. *Proc. Natl. Acad. Sci.* **2014**, *111* (16), 5802–5807.

(37) Bian, Q.; May, A. A.; Kreidenweis, S. M.; Pierce, J. R. Investigation of particle and vapor wall-loss effects on controlled wood-smoke smog-chamber experiments. *Atmospheric Chem. Phys.* **2015**, *15* (19), 11027–11045.

(38) Krechmer, J. E.; Pagonis, D.; Ziemann, P. J.; Jimenez, J. L. Quantification of Gas-Wall Partitioning in Teflon Environmental Chambers Using Rapid Bursts of Low-Volatility Oxidized Species Generated in Situ. *Environ. Sci. Technol.* **2016**, *50* (11), 5757–5765.

(39) Saha, P. K.; Grieshop, A. P. Exploring Divergent Volatility Properties from Yield and Thermodenuder Measurements of Secondary Organic Aerosol from α-Pinene Ozonolysis. *Environ. Sci. Technol.* **2016**, *50* (11), 5740–5749.

(40) Hennigan, C. J.; Miracolo, M. A.; Engelhart, G. J.; May, A. A.; Presto, A. A.; Lee, T.; Sullivan, A. P.; McMeeking, G. R.; Coe, H.; Wold, C. E.; et al. Chemical and physical transformations of organic aerosol from the photo-oxidation of open biomass burning emissions in an environmental chamber. *Atmospheric Chem. Phys.* **2011**, *11* (15), 7669–7686.

(41) Ortega, A. M.; Day, D. A.; Cubison, M. J.; Brune, W. H.; Bon, D.; de Gouw, J. A.; Jimenez, J. L. Secondary organic aerosol formation and primary organic aerosol oxidation from biomass-burning smoke in a flow reactor during FLAME-3. *Atmospheric Chem. Phys.* **2013**, *13* (22), 11551–11571.

(42) Grieshop, A. P.; Logue, J. M.; Donahue, N. M.; Robinson, A. L. Laboratory investigation of photochemical oxidation of organic aerosol from wood fires 1: measurement and simulation of organic aerosol evolution. *Atmospheric Chem. Phys.* **2009**, *9* (4), 1263–1277.

(43) Heringa, M. F.; DeCarlo, P. F.; Chirico, R.; Tritscher, T.; Dommen, J.; Weingartner, E.; Richter, R.; Wehrle, G.; Prévôt, A. S. H.; Baltensperger, U. Investigations of primary and secondary particulate matter of different wood combustion appliances with a high-resolution time-of-flight aerosol mass spectrometer. *Atmospheric Chem. Phys.* **2011**, *11* (12), 5945–5957.

(44) Bruns, E. A.; El Haddad, I.; Keller, A.; Klein, F.; Kumar, N. K.; Pieber, S. M.; Corbin, J. C.; Slowik, J. G.; Brune, W. H.; Baltensperger, U.; et al. Inter-comparison of laboratory smog chamber and flow reactor systems on organic aerosol yield and composition. *Atmospheric Meas. Tech.* **2015**, *8* (6), 2315–2332.

(45) Kang, E.; Toohey, D. W.; Brune, W. H. Dependence of SOA oxidation on organic aerosol mass concentration and OH exposure: experimental PAM chamber studies. *Atmospheric Chem. Phys.* **2011**, *11* (4), 1837–1852.

(46) Lambe, A. T.; Ahern, A. T.; Williams, L. R.; Slowik, J. G.; Wong, J. P. S.; Abbatt, J. P. D.; Brune, W. H.; Ng, N. L.; Wright, J. P.; Croasdale, D. R.; et al. Characterization of aerosol photooxidation flow reactors: heterogeneous oxidation, secondary organic aerosol formation and cloud condensation nuclei activity measurements. *Atmospheric Meas. Tech.* **2011**, *4* (3), 445–461.

(47) Lambe, A. T.; Onasch, T. B.; Massoli, P.; Croasdale, D. R.; Wright, J. P.; Ahern, A. T.; Williams, L. R.; Worsnop, D. R.; Brune, W. H.; Davidovits, P. Laboratory studies of the chemical composition and cloud condensation nuclei (CCN) activity of secondary organic aerosol (SOA) and oxidized primary organic aerosol (OPOA). *Atmospheric Chem. Phys.* **2011**, *11* (17), 8913–8928.

(48) Lambe, A. T.; Onasch, T. B.; Croasdale, D. R.; Wright, J. P.; Martin, A. T.; Franklin, J. P.; Massoli, P.; Kroll, J. H.; Canagaratna, M. R.; Brune, W. H.; et al. Transitions from Functionalization to Fragmentation Reactions of Laboratory Secondary Organic Aerosol (SOA) Generated from the OH Oxidation of Alkane Precursors. *Environ. Sci. Technol.* **2012**, *46* (10), 5430–5437.

(49) Lee, S.; Kim, H. K.; Yan, B.; Cobb, C. E.; Hennigan, C.; Nichols, S.; Chamber, M.; Edgerton, E. S.; Jansen, J. J.; Hu, Y.; et al. Diagnosis of Aged Prescribed Burning Plumes Impacting an Urban Area. *Environ. Sci. Technol.* **2008**, *42* (5), 1438–1444.

(50) Yokelson, R. J.; Crounse, J. D.; DeCarlo, P. F.; Karl, T.; Urbanski, S.; Atlas, E.; Campos, T.; Shinozuka, Y.; Kapustin, V.; Clarke, A. D.; et al. Emissions from biomass burning in the Yucatan. *Atmospheric Chem. Phys.* **2009**, *9* (15), 5785–5812.

(51) DeCarlo, P. F.; Ulbrich, I. M.; Crounse, J.; de Foy, B.; Dunlea, E. J.; Aiken, A. C.; Knapp, D.; Weinheimer, A. J.; Campos, T.; Wennberg, P. O.; et al. Investigation of the sources and processing of organic aerosol over the Central Mexican Plateau from aircraft measurements during MILAGRO. *Atmospheric Chem. Phys.* **2010**, *10* (12), 5257–5280.

(52) Vakkari, V.; Kerminen, V.-M.; Beukes, J. P.; Tiitta, P.; van Zyl, P. G.; Josipovic, M.; Venter, A. D.; Jaars, K.; Worsnop, D. R.; Kulmala, M.; et al. Rapid changes in biomass burning aerosols by atmospheric oxidation. BURNING PLUMES. *Geophys. Res. Lett.* **2014**, *41* (7), 2644–2651.

(53) Capes, G.; Johnson, B.; McFiggans, G.; Williams, P. I.; Haywood, J.; Coe, H. Aging of biomass burning aerosols over West Africa: Aircraft measurements of chemical composition, microphysical properties, and emission ratios. *J. Geophys. Res.* **2008**, *113*.

(54) Cubison, M. J.; Ortega, A. M.; Hayes, P. L.; Farmer, D. K.; Day, D.; Lechner, M. J.; Brune, W. H.; Apel, E.; Diskin, G. S.; Fisher, J. A.; et al. Effects of aging on organic

aerosol from open biomass burning smoke in aircraft and laboratory studies. *Atmospheric Chem. Phys.* **2011**, *11* (23), 12049–12064.

(55) Akagi, S. K.; Craven, J. S.; Taylor, J. W.; McMeeking, G. R.; Yokelson, R. J.; Burling, I. R.; Urbanski, S. P.; Wold, C. E.; Seinfeld, J. H.; Coe, H.; et al. Evolution of trace gases and particles emitted by a chaparral fire in California. *Atmospheric Chem. Phys.* **2012**, *12* (3), 1397–1421.

(56) Reid, J. S.; Koppmann, R.; Eck, T. F.; Eleuterio, D. P. A review of biomass burning emissions part II: intensive physical properties of biomass burning particles. *Atmospheric Chem. Phys.* **2005**, *5* (3), 799–825.

(57) Aung, T. W.; Jain, G.; Sethuraman, K.; Baumgartner, J.; Reynolds, C.; Grieshop, A. P.; Marshall, J. D.; Brauer, M. Health and Climate-Relevant Pollutant Concentrations from a Carbon-Finance Approved Cookstove Intervention in Rural India. *Environ. Sci. Technol.* **2016**, *50* (13), 7228–7238.

(58) Grieshop, A.; Jain, G.; Sethuraman, K.; Marshall, J. In-home emission factors of climate- and health-relevant pollutants measured during a carbon-finance approved cookstove intervention in rural India. *GeoHealth* **2017**.

(59) Mortimer, K.; Ndamala, C. B.; Naunje, A. W.; Malava, J.; Katundu, C.; Weston, W.; Havens, D.; Pope, D.; Bruce, N. G.; Nyirenda, M.; et al. A cleaner burning biomass-fuelled cookstove intervention to prevent pneumonia in children under 5 years old in rural Malawi (the Cooking and Pneumonia Study): a cluster randomised controlled trial. *The Lancet* **2016**.

(60) Weston, W.; Smedley, J.; Bennett, A.; Mortimer, K. The Cooking and Pneumonia Study (CAPS) in Malawi: Implementation of Remote Source Data Verification. *PLOS ONE* **2016**, *11* (6), e0155966.

(61) Wathore, R.; Mortimer, K.; Grieshop, A. P. In-use emissions and estimated impacts of traditional, natural- and forced-draft cookstoves in rural Malawi. *Environ. Sci. Technol.* **2017**.

(62) Bailis, P. R.; Ogle, D.; Maccarty, N.; From, D. S. I.; Smith, K. R.; Edwards, R.; Energy, H.; Programme, H.; Foundation, S. *The Water Boiling Test (WBT)*; 2007.

(63) Johnson, M.; Edwards, R.; Alatorre Frenk, C.; Masera, O. In-field greenhouse gas emissions from cookstoves in rural Mexican households. *Atmos. Environ.* **2008**, *42* (6), 1206–1222.

(64) Repoff, R. Bringing the Kitchen to the Lab: Data Analysis and Method Development for Lab Simulation of In-Field Operation of Biomass Cookstoves, North Carolina State Univerisity, 2015.

(65) Ng, N. L.; Herndon, S. C.; Trimborn, A.; Canagaratna, M. R.; Croteau, P. L.; Onasch, T. B.; Sueper, D.; Worsnop, D. R.; Zhang, Q.; Sun, Y. L.; et al. An Aerosol Chemical Speciation Monitor (ACSM) for Routine Monitoring of the Composition and Mass Concentrations of Ambient Aerosol. *Aerosol Sci. Technol.* **2011**, *45* (7), 780–794.

(66) Saleh, R.; Hennigan, C. J.; McMeeking, G. R.; Chuang, W. K.; Robinson, E. S.; Coe, H.; Donahue, N. M.; Robinson, A. L. Absorptivity of brown carbon in fresh and photo-chemically aged biomass-burning emissions. *Atmospheric Chem. Phys.* **2013**, *13* (15), 7683–7693.

(67) Bond, T. C.; Anderson, T. L.; Campbell, D. Calibration and Intercomparison of Filter-Based Measurements of Visible Light Absorption by Aerosols. *Aerosol Sci. Technol.* **1999**, *30* (6), 582–600.

(68) Grieshop, A. P.; Donahue, N. M.; Robinson, A. L. Is the gas-particle partitioning in alpha-pinene secondary organic aerosol reversible? *Geophys. Res. Lett.* **2007**, *34*, L14810.

(69) Weitkamp, E. A.; Sage, A. M.; Pierce, J. R.; Donahue, N. M.; Robinson, A. L. Organic Aerosol Formation from Photochemical Oxidation of Diesel Exhaust in a Smog Chamber. *Environ. Sci. Technol.* **2007**, *41* (20), 6969–6975.

(70) Kang, E.; Root, M. J.; Toohey, D. W.; Brune, W. H. Introducing the concept of Potential Aerosol Mass (PAM). *Atmospheric Chem. Phys.* **2007**, *7* (22), 5727–5744.

(71) Li, R.; Palm, B. B.; Ortega, A. M.; Hlywiak, J.; Hu, W.; Peng, Z.; Day, D. A.; Knote, C.; Brune, W. H.; de Gouw, J. A.; et al. Modeling the Radical Chemistry in an Oxidation Flow Reactor: Radical Formation and Recycling, Sensitivities, and the OH Exposure Estimation Equation. *J. Phys. Chem. A* **2015**, 150406123535006.

(72) Peng, Z.; Day, D. A.; Ortega, A. M.; Palm, B. B.; Hu, W.; Stark, H.; Li, R.; Tsigaridis, K.; Brune, W. H.; Jimenez, J. L. Non-OH chemistry in oxidation flow reactors for the study of atmospheric chemistry systematically examined by modeling. *Atmospheric Chem. Phys.* **2016**, *16* (7), 4283–4305.

(73) Aiken, A. C.; DeCarlo, P. F.; Jimenez, J. L. Elemental Analysis of Organic Species with Electron Ionization High-Resolution Mass Spectrometry. *Anal. Chem.* **2007**, *79* (21), 8350–8358.

(74) Aiken, A. C.; DeCarlo, P. F.; Kroll, J. H.; Worsnop, D. R.; Huffman, J. A.; Docherty, K. S.; Ulbrich, I. M.; Mohr, C.; Kimmel, J. R.; Sueper, D.; et al. O/C and OM/OC Ratios of Primary, Secondary, and Ambient Organic Aerosols with High-Resolution Time-of-Flight Aerosol Mass Spectrometry. *Environ. Sci. Technol.* **2008**, *42* (12), 4478–4485.

(75) Canagaratna, M. R.; Jimenez, J. L.; Kroll, J. H.; Chen, Q.; Kessler, S. H.; Massoli, P.; Hildebrandt Ruiz, L.; Fortner, E.; Williams, L. R.; Wilson, K. R.; et al. Elemental ratio measurements of organic compounds using aerosol mass spectrometry: characterization,

improved calibration, and implications. *Atmospheric Chem. Phys. Discuss.* **2014**, *14* (13), 19791–19835.

(76) Zhang, Q.; Alfarra, M. R.; Worsnop, D. R.; Allan, J. D.; Coe, H.; Canagaratna, M. R.; Jimenez, J. L. Deconvolution and Quantification of Hydrocarbon-like and Oxygenated Organic Aerosols Based on Aerosol Mass Spectrometry. *Environ. Sci. Technol.* **2005**, *39* (13), 4938–4952.

(77) Zhang, Q.; Worsnop, D. R.; Canagaratna, M. R.; Jimenez, J. L. Hydrocarbon-like and oxygenated organic aerosols in Pittsburgh: insights into sources and processes of organic aerosols. *Atmospheric Chem. Phys.* **2005**, *5* (12), 3289–3311.

(78) Schneider, J.; Weimer, S.; Drewnick, F.; Borrmann, S.; Helas, G.; Gwaze, P.; Schmid, O.; Andreae, M. O.; Kirchner, U. Mass spectrometric analysis and aerodynamic properties of various types of combustion-related aerosol particles. *Int. J. Mass Spectrom.* **2006**, *258* (1–3), 37–49.

(79) Alfarra, M. R.; Prevot, A. S. H.; Szidat, S.; Sandradewi, J.; Weimer, S.; Lanz, V. A.; Schreiber, D.; Mohr, M.; Baltensperger, U. Identification of the Mass Spectral Signature of Organic Aerosols from Wood Burning Emissions. *Environ. Sci. Technol.* **2007**, *41* (16), 5770–5777.

(80) Corbin, J. C.; Keller, A.; Lohmann, U.; Burtscher, H.; Sierau, B.; Mensah, A. A. Organic Emissions from a Wood Stove and a Pellet Stove Before and After Simulated Atmospheric Aging. *Aerosol Sci. Technol.* **2015**, *49* (11), 1037–1050.

(81) Tiitta, P.; Leskinen, A.; Hao, L.; Yli-Pirilä, P.; Kortelainen, M.; Grigonyte, J.; Tissari, J.; Lamberg, H.; Hartikainen, A.; Kuuspalo, K.; et al. Transformation of logwood combustion emissions in a smog chamber: formation of secondary organic aerosol and changes in the primary organic aerosol upon daytime and nighttime aging. *Atmospheric Chem. Phys. Discuss.* **2016**, 1–38.

(82) Weimer, S.; Alfarra, M. R.; Schreiber, D.; Mohr, M.; Prévôt, A. S. H.; Baltensperger, U. Organic aerosol mass spectral signatures from wood-burning emissions: Influence of burning conditions and wood type. *J. Geophys. Res.* **2008**, *113* (D10).

(83) Elsasser, M.; Busch, C.; Orasche, J.; Schön, C.; Hartmann, H.; Schnelle-Kreis, J.; Zimmermann, R. Dynamic Changes of the Aerosol Composition and Concentration during Different Burning Phases of Wood Combustion. *Energy Fuels* **2013**, *27* (8), 4959–4968.

(84) Jolleys, M. D.; Coe, H.; McFiggans, G.; McMeeking, G. R.; Lee, T.; Kreidenweis, S. M.; Collett, J. L.; Sullivan, A. P. Organic aerosol emission ratios from the laboratory combustion of biomass fuels: BBOA emission ratios in chamber studies. *J. Geophys. Res. Atmospheres* **2014**, *119* (22), 12,850-12,871.

(85) Bruns, E. A.; Krapf, M.; Orasche, J.; Huang, Y.; Zimmermann, R.; Drinovec, L.; Močnik, G.; El-Haddad, I.; Slowik, J. G.; Dommen, J.; et al. Characterization of primary and secondary wood combustion products generated under different burner loads. *Atmospheric Chem. Phys.* **2015**, *15* (5), 2825–2841.

(86) Bruns, E. A.; El Haddad, I.; Slowik, J. G.; Kilic, D.; Klein, F.; Baltensperger, U.; Prévôt, A. S. H. Identification of significant precursor gases of secondary organic aerosols from residential wood combustion. *Sci. Rep.* **2016**, *6*, 27881.

(87) Hennigan, C. J.; Sullivan, A. P.; Collett, J. L.; Robinson, A. L. Levoglucosan stability in biomass burning particles exposed to hydroxyl radicals: LEVOGLUCOSAN STABILITY IN AEROSOL. *Geophys. Res. Lett.* **2010**, *37* (9), n/a-n/a.

(88) Grieshop, A. P.; Donahue, N. M.; Robinson, A. L. Laboratory investigation of photochemical oxidation of organic aerosol from wood fires 2: analysis of aerosol mass spectrometer data. *Atmospheric Chem. Phys.* **2009**, *9* (6), 2227–2240.

(89) Heald, C. L.; Kroll, J. H.; Jimenez, J. L.; Docherty, K. S.; DeCarlo, P. F.; Aiken, A. C.; Chen, Q.; Martin, S. T.; Farmer, D. K.; Artaxo, P. A simplified description of the evolution of organic aerosol composition in the atmosphere: VAN KREVELEN DIAGRAM OF ORGANIC AEROSOL. *Geophys. Res. Lett.* **2010**, *37* (8), n/a-n/a.

(90) Ng, N. L.; Canagaratna, M. R.; Jimenez, J. L.; Chhabra, P. S.; Seinfeld, J. H.; Worsnop, D. R. Changes in organic aerosol composition with aging inferred from aerosol mass spectra. *Atmospheric Chem. Phys.* **2011**, *11* (13), 6465–6474.

(91) Kim, S.; Kramer, R. W.; Hatcher, P. G. Graphical Method for Analysis of Ultrahigh-Resolution Broadband Mass Spectra of Natural Organic Matter, the Van Krevelen Diagram. *Anal. Chem.* **2003**, *75* (20), 5336–5344.

(92) Podgorski, D. C.; Hamdan, R.; McKenna, A. M.; Nyadong, L.; Rodgers, R. P.; Marshall, A. G.; Cooper, W. T. Characterization of Pyrogenic Black Carbon by Desorption Atmospheric Pressure Photoionization Fourier Transform Ion Cyclotron Resonance Mass Spectrometry. *Anal. Chem.* **2012**, *84* (3), 1281–1287.

(93) Gunarathne, D. S.; Mueller, A.; Fleck, S.; Kolb, T.; Chmielewski, J. K.; Yang, W.; Blasiak, W. Gasification Characteristics of Hydrothermal Carbonized Biomass in an Updraft Pilot-Scale Gasifier. *Energy Fuels* **2014**, *28* (3), 1992–2002.

(94) Reza, M. T.; Andert, J.; Wirth, B.; Busch, D.; Pielert, J.; Lynam, J. G.; Mumme, J. Hydrothermal Carbonization of Biomass for Energy and Crop Production. *Appl. Bioenergy* **2014**, *1* (1).

(95) Martinsson, J.; Eriksson, A. C.; Nielsen, I. E.; Malmborg, V. B.; Ahlberg, E.; Andersen, C.; Lindgren, R.; Nyström, R.; Nordin, E. Z.; Brune, W. H.; et al. Impacts of Combustion Conditions and Photochemical Processing on the Light Absorption of Biomass Combustion Aerosol. *Environ. Sci. Technol.* **2015**.

(96) Saliba, G.; Subramanian, R.; Saleh, R.; Ahern, A. T.; Lipsky, E. M.; Tasoglou, A.; Sullivan, R. C.; Bhandari, J.; Mazzoleni, C.; Robinson, A. L. Optical properties of black carbon in cookstove emissions coated with secondary organic aerosols: Measurements and modeling. *Aerosol Sci. Technol.* **2016**, *50* (11), 1264–1276.

(97) Bergstrom, R. W.; Russell, P. B.; Hignett, P. Wavelength Dependence of the Absorption of Black Carbon Particles: Predictions and Results from the TARFOX Experiment and Implications for the Aerosol Single Scattering Albedo. *J. Atmospheric Sci.* **2002**, *59* (3), 567–577.

(98) Schnaiter, M. Absorption amplification of black carbon internally mixed with secondary organic aerosol. *J. Geophys. Res.* **2005**, *110* (D19).

(99) Kirchstetter, T. W.; Novakov, T.; Hobbs, P. V. Evidence that the spectral dependence of light absorption by aerosols is affected by organic carbon: SPECTRAL LIGHT ABSORPTION BY AEROSOLS. *J. Geophys. Res. Atmospheres* **2004**, *109* (D21), n/a-n/a.

(100) Zhong, M.; Jang, M. Dynamic light absorption of biomass-burning organic carbon photochemically aged under natural sunlight. *Atmospheric Chem. Phys.* **2014**, *14* (3), 1517–1525.

(101) Park, S. S.; Yu, J. Chemical and light absorption properties of humic-like substances from biomass burning emissions under controlled combustion experiments. *Atmos. Environ.* **2016**, *136*, 114–122.

(102) Kirchstetter, T. W.; Thatcher, T. L. Contribution of organic carbon to wood smoke particulate matter absorption of solar radiation. *Atmospheric Chem. Phys.* **2012**, *12* (14), 6067–6072.

(103) Zhong, M.; Jang, M. Light absorption coefficient measurement of SOA using a UV–Visible spectrometer connected with an integrating sphere. *Atmos. Environ.* **2011**, *45* (25), 4263–4271.

(104) Palm, B. B.; Campuzano-Jost, P.; Ortega, A. M.; Day, D. A.; Kaser, L.; Jud, W.; Karl, T.; Hansel, A.; Hunter, J. F.; Cross, E. S.; et al. In situ secondary organic aerosol formation from ambient pine forest air using an oxidation flow reactor. *Atmospheric Chem. Phys.* **2016**, *16* (5), 2943–2970.

APPENDICES

APPENDIX A

Section A1. Instruments

The instrumentation used in this study is shown in Figure A2 and summarized in Table A1. Diluted primary emissions from the cookstoves were sampled directly from the duct by the Stove Emission Measurement System (STEMS-1G)[1] during the burn. The STEMS measures CO, CO_2, aerosol light scattering (wavelength $\lambda = 635$ nm), temperature, and RH in real time and uses a microaethlometer to measure aerosol light absorption at $\lambda = 880$ nm. It also collects integrated filter samples as described below. Downstream of the STEMS and upstream of the F-OFR gas-phase instruments measured unaged primary emissions during both online and batch configurations.

A range of aerosol particle instrumentation measured downstream of the F-OFR: a scanning mobility particle sizer (SMPS, TSI Inc., CPC 3787/DMA 3081 operated with a sheath flow of 3.0 LPM and aerosol flow of 0.6 LPM) measured aerosol size distribution (15–685 nm), an aerosol chemical speciation monitor (ACSM, Aerodyne Research Inc; 75 – 650 nm) measured aerosol composition and mass concentrations[2], a photoacoustic extinctiometer measured particle absorption and scattering at $\lambda = 870$ nm (PAX, Droplet Measurement). A 3-λ (470, 522, and 660nm) particle soot absorption photometer (PSAP; Radiance Research) was used to quantify wavelength-dependence of absorption[3], but not BC concentrations due to loading/scattering filter artifacts[4]. Zero air metered by a mass-flow-controller was used to additionally dilute (~dilution ratio 10-20) the PSAP sample to minimize filter-changes. Downstream of the F-OFR, gas-phase instruments continuously measured CO (48i Thermo Fisher Scientific), O_3 (205 2B

Technologies), CO_2 (LI-820 LI-COR) in photo-chemically aged emissions during online and batch sampling.

Primary emissions from the duct and aged emissions downstream of the F-OFR were simultaneously collected during online sampling on quartz and Teflon filters in the STEMS (at 2.5 l min^{-1}) and at 1.2 l min^{-1} using an impactor with a 2.5 µm cutoff, respectively. In both, one filter holder contained a 47 mm bare quartz filter (BareQ) and the other filter holder contained a 47 mm quartz filter behind a Teflon filter (QBT filter) used to correct for OC positive artifacts from gas phase organics[5]. Quartz filters were analyzed with a Sunset Labs Organic and Elemental Carbon (OC/EC) analyzer to quantify elemental (EC) and organic carbon (OC). Teflon filters were weighed before and after experiments using a Mettler-Toledo UMX-2 microbalance in a T/RH-controlled chamber to quantify the total $PM_{2.5.}$

Section A2. Data Analysis: Corrections

Several corrections were applied to data to allow for measurements at different locations and times to be compared to assess evolution of emissions. These corrections account for particle loss through the F-OFR, particle loss to the smog chamber walls, and ACSM transmission window limitations. Particle loss through the F-OFR was determined, assuming that BC acts as an inert tracer, from the fraction of absorption measured by the PAX downstream of the OFR to that expected based on the exponential fit of bypass measurements in the smog chamber. This correction was applied to the F-OFR measurements for each OH exposure on a per test basis. The variability of the loss characterization is shown in Figure A10 using a box and whisker plot [5th 25th 50th 75th 95th percentiles] across a range of average OH exposures binned by approximately 1.5 equivalent days of aging. The average loss at each average OH exposure is shown with a green marker. The trend in particle loss across OH exposures during batch sampling was used to estimate an appropriate correction for the OH exposure during online sampling. A slight increase in the fraction lost was observed with increasing OH exposures. The exact reason for this increase is not known but similar losses were measured with the PSAP, suggesting that this loss is real and not a measurement artifact due to variations in temperature, relative humidity or gas-phase concentrations. Possible explanations include electrostatic interference, thermophoresis, and/or changes in particle morphology or coating. The UV bulbs could be creating interference due to the electric field imposed by the UV bulbs or possibly creating a temperature gradient between the bulbs and the reactor walls. Also, the morphology and coating of BC particles may be changing due to the condensation of semi-volatile vapors. At high OH exposures, these effects might be more pronounced because a second UV bulb is required to be powered to achieve necessary oxidant concentrations. However, these corrections are relatively minor and do not affect the overall conclusions of the study.

Based on similar wood smoke characterization and aging experiments an ACSM collection efficiency of 1 was assumed[2,6–8]. As noted below (Figure A4), this leads to a good agreement between filter-based OC and OA measured via the ACSM. To attempt to account for the POA in a way that is consistent across instrument particle size measurement ranges, loading in the chamber was corrected for mass outside the ACSM transmission window (75-650 nm) designated by the dashed lines in Figure A11[9]. SMPS volume distributions of the initial loading in the smog chamber were fitted for diameters between 0.6 and 1000 nm. The estimated fraction of SMPS-measured aerosol volume (assuming spherical particles) not detected by the ACSM was determined on a per test basis for each cookstove. The average fraction of aerosol volume outside of this range for the TSF, Chulika, and Philips was 43%, 71%, and 56%, respectively. This correction is not applied to the mass enhancement (delta_OA) measured during OFR aging, as the vast majority of SOA condensation in the F-OFR was observed to occur within the ACSM transmission window. The green points in panel b for each cookstove model show aged volume distributions. If significant formation is occurring below the detection window of the ACSM then these results would be considered a lower estimate of OA production.

POA was also corrected for smog chamber particle wall loss during the loading period referred to as POA at batch$_{t=0}$. Light scattering and absorption measured by the STEMS were used to estimate the real-time transfer rate of aerosol to the smog chamber. Using a first order loss coefficient for particle-wall-loss (slope of exponential decay rate of absorption measured during bypass batch sampling) the concentration of particles lost to the chamber walls during the loading period was determined. The ratio of the sum of particles loss to the chamber walls to the sum of emitted particles during the burn determined the percentage PM (scattering) and BC (absorption) loss. These corrections were only applied to the POA concentration in the chamber in order to account for primary OA mass captured by filters. Figure A4 compares the primary OM EFs measured by the STEMs to chamber POA loadings at batch$_{t=0}$. OC collected on the filters was converted to OM EFs using the Improved-Ambient' parameterization based on unaged f43 and f44[15–17]. A liner regression showed the chamber OA EFs agreed well ($R^2 = 0.87$) with the primary filter-based OM EFs with a slope of 0.84 ± .10 after applying corrections.

Section A3. Model Parameterization

The model used to estimate the OH exposure offline is based on the work by Li et al. (2015) designed for the PAM reactor[10] but with parameters fitted based on a characterization of our flow tube reactor. The equation used is:

$$\text{Eq. A1}\quad \log(OH_{exp}) = a + \left(b + c \times OHR^{d} + e \times \log(O_3) * OHR^{f}\right) \times \log(O_3) + \log(H_2O) + \log(\frac{t}{82})$$

O_3 is the ozone concentration (molecules cm^{-3}), H_2O is the water vapor mixing ratio (%), t is the residence time in the reactor (s), and OHR is the external OH reactivity (s^{-1}). The model-estimated OH exposure was adjusted for a difference in residence time between the model (82 seconds), the ambient study (70 seconds), and the current study (54-68 seconds). The parameters (a-f) were obtained by fitting the above equation to data collected during operation of the F-OFR across a range of conditions of varying bulb setting, water mixing ratio and OHR. The model-fitting data set is shown with red markers in Figure A12. OHR and H_2O were varied by introducing excess CO and water into the sample stream. Additional external OHR competes for OH in the reactor, and thus suppresses OH oxidation relative to low-OHR conditions. In this study, OH exposure was suppressed due to the elevated OHR of the relatively highly concentrated cookstove emissions. Since detailed VOC measurements were not collected during cookstove experiments, the OHR of these emissions were estimated from VOC/CO ratios of woodland oak measured during Flame III[11] scaled by the CO concentration measured upstream of the F-OFR. OH exposures using the adjusted OHR values are compared to model estimates for previous laboratory and field measurements in Figure A12. The OH exposure determined from the model is compared against ambient measurements from a near road (I-40) campaign that used a CO tracer to determine the OH exposure online, shown by the blue markers. The OH exposure measured using the tracer decay agrees well with the model output for all of these data sets, with the greatest observed difference occurring at low exposures. This indicates that our F-OFR is performing consistently with other OFR versions and that OH exposure is reasonably well described by this model formulation.

Section A4. Organic Particle Signal at *m/z* 28

Typically, the ACSM signal at *m/z* 28 (N_2^+) is associated with the airbeam and the organic contribution is assumed to be zero in the fragmentation table[12]. However, recent analysis suggests there is a substantial particle phase contribution to OA at *m/z* 28[13–15]. The Aiken et al. fragmentation table sets the organic contribution at *m/z* 28 equivalent to the signal at *m/z* 44, but this does not affect the total organic mass because it decreases the contribution at *m/z* 18[15]. Overall, we found evidence that there is a substantial OA contribution at m/z 28, but that due to signal-to-noise limitations in the ACSM, we were not able to consistently quantify this contribution. For this reason, we have chosen to use the default ACSM fragmentation table, which neglects contribution to OA at m/z 28 (e.g. CO^+ fragments). This may lead to a small under-estimation of OA mass. Figure A13 shows the ratio of the difference (unfilter minus filtered MS) signal at *m/z* 28 and *m/z* 44. An example mass spectra (MS) segment is also shown for TSF-062916, in which the difference signal at *m/z* 28 is roughly equivalent to that at *m/z* 44. Due to the inability to separate the organic particle signal from the dominating airbeam signal at lower POA concentrations, the contribution at *m/z* 28 was not used to calculate the total organics. The MS segment for NDS-082516 shows a negative signal at *m/z* 28 indicating noise from the airbeam is dominating the signal.

Section A5. Estimating Elemental Ratios from ACSM Mass Spectra

To extend the evaluation of OA composition, atomic ratios (H:C; O:C) were estimated using the 'Improved-Ambient' parameterization based on f43 and f44 measured during batch sampling[15–17]. This likely provides a slightly high-biased estimate of H:C and O:C because the ACSM *m/z* range is truncated (to *m/z* 150) relative to the Aerosol Mass Spectrometers (AMS; to *m/z* 300) used to devise the parameterization. AMS wood-smoke spectra[18] suggest that approximately 90% and 95% of fresh POA and aged OA is contributed at <150 amu. Based on the parameterization, this truncation may contribute to ~10% and ~5% overestimations of O:C and H:C, respectively. Further, Ortega et al. showed that the 'Ambient' O:C parameterization underestimated O:C determined using elemental analysis of high-resolution wood-smoke spectra[14]. Therefore, we here provide 'estimated' elemental ratios and suggest that while the observed trends are likely captured with this approach, there is substantial (10-20%) uncertainty in the absolute values of elemental ratios. It should also be noted that the f44 value for the FDGS is at the upper end of data used to develop the parameterization, and so FDGS elemental ratios should especially be considered cautiously. Future work should examine OA from these sources with higher resolution instruments capable of resolving elemental contributions.

Section A6. H:C and O:C Including Refractory Carbon

O:C and H:C ratios were adjusted to include the contribution from refractory carbon in a Van Krevelen plot framework to consider the evolution of carbonaceous material during the combustion of biomass. Equations A2, A3, and A4 were used to estimate the mass emission factors of OA-associated oxygen, hydrogen, and carbon on a per fuel basis.

$$\text{Eq. A2} \quad \frac{g\ O\ (OA)}{kg\ of\ fuel} = \frac{O}{C} * \frac{1\ mole\ C}{12\ g\ C} * \frac{16\ g\ O}{1\ mole\ O} * \frac{g\ OA}{kg\ of\ fuel} * \frac{OC}{OM}$$

Eq. A3 $$\frac{g\ H\ (OA)}{kg\ of\ fuel} = \frac{H}{C} * \frac{1\ mole\ C}{12\ g\ C} * \frac{1\ g\ H}{1\ mole\ H} * \frac{g\ OA}{kg\ of\ fuel} * \frac{OC}{OM}$$

Eq. A4 $$\frac{g\ C\ (OA)}{kg\ of\ fuel} = \frac{g\ OA}{kg\ of\ fuel} * \frac{OC}{OM}$$

In equations A2-A4, grams of OA per kg of fuel is quantified by the POA EF for unaged emissions and as total OA (POA + SOA) EF for aged emissions, corrected for ACSM lens transmission limits for POA (as discussed in Section A2 above). The OC/OM ratio corresponds to the values for unaged/aged emissions shown in Tables A2 and A3. To account for refractory carbon, BC EFs measured by the PAX using a MAC of 3.33 $m^2\ g^{-1}$ (calculated using a regression fit between EC and BC; Figure A6) was added to the OA carbon EFs calculated using equation A3. O:C and H:C ratios were then recalculated on a molar basis.

Section A7. Optical Properties

Real-time aerosol optical properties were examined across stove type to provide additional understanding of the environmental impacts of cookstoves. Single scattering albedo (SSA) quantifies the ratio of scattering to total extinction using the absorption (b_{abs}, Mm^{-1}) and scattering (b_{scat}, Mm^{-1}) measured at 870 nm by the PAX (b_{scat} /(b_{abs}+b_{scat})). A lower SSA is indicative of particles that are more light-absorbing. Unaged emissions from the TSF, NDS, and FDGS had test average (±1 σ) SSA values of 0.62±0.14, 0.24±0.02 and 0.17±0.02 respectively. All three of these values are below the climate cooling-to-warming threshold of .85[19], suggesting the POA from all stoves have direct climate warming effects, though including indirect effects may mitigate the overall impact. While all the stoves emit strongly absorbing particles, particles from the alternative stoves on average have 50% greater contribution of absorption to total extinction. However, both alternative stoves have lower PM EFs than the TSF and also have a greater thermal efficiency[20], complicating the direct connection from stove use to climate impacts. Figure A8A shows the average peak SSA for each stove type after OH exposure. The data show a trend of increasing SSA with OH exposure indicating aerosols are becoming more light-scattering. This is consistent with other studies that have shown SSA increases with the enhancement of OC[21,22]. Figure A8B shows as MCE increases particles become less light scattering. Similarly, A8C shows as SSA decreases a greater fraction of TC consists of EC.

A power law was used to fit PSAP b_{abs} measurements across 467, 530, and 660 nm wavelengths and the slope was used to derive the Absorption Angstrom exponent (AAE). The absorption at 870 nm was extrapolated and assumed to be pure BC. The BC contribution across 467, 530, and 660 nm wavelengths was determined using a power law fit with an exponent of 1. The difference between the measured absorption at a wavelength and the expected contribution from black carbon is called the BrC fraction of the total absorption[23].

Section A8. Modeled Fate of LVOCs in Oxidation Flow Reactor

Recent research using the PAM reactor[24] has explored the fate of low volatility organic compounds (LVOC) that form in the reactor to assess the possible influence of vapor wall loss or kinetic limitations on observed enhancement. We modeled the most important chemical pathways following the approach of Palm et al.,[24] as shown in Figure A10A. The potential fate of an LVOC in the F-OFR includes: condensing on particle surface area, condensation to the walls of the reactor, reacting with OH radicals 5+ times at which point it is considered ‘incondensable’, or exiting the F-OFR as a vapor. Figure A10A shows that, due to the large concentration of particles in these experiments, the dominating pathway was condensation onto the surface area of particles. For experiments with lower particle surface area concentrations, the other significant pathway was reacting with OH radicals 5+ times. Condensation to the F-OFR reactor walls and vapors exiting the reactor had a minimal influence due to a short residence time and low wall surface area relative to the particle surface area.

A negative consequence of the higher concentrations of emissions in our experiments is the possible contribution of non-OH radical chemistry in the reactor. High concentrations result in elevated levels of external OHR (179-742 s^{-1}), which leads to a suppression of OH radicals and the dominance of less-atmospherically-relevant chemistry (e.g. UV photolysis). Recent modeling with the PAM reactor has defined regimes based environmental parameters to determine if chemistry in the reactor is atmospherically relevant[25], as shown in Figure 13B. Figure 13B demonstrates experiments should be run at relatively lower OHR and higher water mixing ratio[25] to move in to the “safe” regime. Future experiments should attempt to employ additional dilution and/or elevated RH levels to increase the relative importance of OH radical in OFR chemistry.

Table A1. Summary of instruments and manufacturers

Measurement Locations	Measurement	Manufacturer
Primary (STEMS)	CO	Alphasense
	CO2	Aprovecho PEMS Board
	Red Laser Scattering Photometer	Aprovecho PEMS Board
	Temperature	SHT15
	Relative Humidity	SHT15
	AE-51 Absorption	AethLabs
Primary (Pre F-OFR)	NO_x	401/410 2B Technologies
	CO	48C Thermo Fisher Scientific
	O_3	106-L 2B Technologies
Primary/Aged (Post F-OFR)	Particle Size Distribution	SMPS (TSI Inc.) CPC 3787/DMA 3081
	aerosol chemical speciation	ACSM (Aerodyne Research Inc.)
	Black carbon absorption/scattering	PAX (DMT Inc.) (λ = 870 nm)
	particle soot absorption photometer	PSAP (Radiance Research) (λ = 470, 522, and 660nm)
Aged (Post F-OFR)	CO	48i Thermo Fisher Scientific
	O_3	205 2B Technologies
	CO_2	LI-820 LI-COR
Primary/Aged (Offline)	EC/OC	Sunset

Table A2. Primary emissions for each experiment measured by the STEMS in the duct during stove tests. Mass of fuel used is the sum of fuel used during the hot start and the simmering phase. The mass of fuel used was unintentionally not recorded for the NDS test on 6/23/16. The MCE, ΔCO, and ΔCO_2 are the average values during the online configuration. ΔCO and ΔCO_2 are background corrected. The EC, OC, and PM EFs are based on primary filters collected by the STEMS. The unaged OM:OC ratio was estimated using the Improved-Ambient method[18–20] based on unaged f_{44} measured during batch bypass sampling.

Test ID	Stove Type	Test Protocol	Fuel Mass Used (g)	MCE	ΔCO (ppm)	ΔCO2 (ppm)	EC EF (g kg^{-1} of fuel)	OC EF (g kg^{-1} of fuel)	PM EF (g kg^{-1} of fuel)	Unaged OM:OC Ratio
62916	TSF	WBT	1054	0.94	87.2	1317.6	0.54	2.96	6.50	1.49
71916	TSF	WBT	1192	0.92	129.6	1428.5	0.64	5.13	10.68	1.47
72916	TSF	MTP	1121	0.92	88.3	1020.3	0.75	2.64	5.82	1.50
80316	TSF	MTP	1267	0.94	87.1	1255.1	0.68	2.08	4.60	1.78
90216	TSF	WBT	1309	0.93	97.7	1368.5	0.50	5.68	12.42	1.44
50216	NDS	WBT	997	0.96	50.0	1192.5	0.79	0.76	3.82	1.72
60616	NDS	WBT	928	0.97	38.2	1146.8	0.91	0.80	3.74	1.99
62316	NDS	WBT	--	0.96	29.9	734.7	1.46	1.01	4.66	--
70716	NDS	WBT	944	0.96	55.3	1370.4	1.32	0.69	2.14	1.75
72216	NDS	MTP	888	0.95	55.0	1095.0	1.72	0.80	3.73	1.90
72616	NDS	MTP	877	0.95	60.9	1081.5	1.39	1.01	3.98	1.85
82516	NDS	WBT	896	0.97	40.2	1196.4	1.25	0.78	3.06	1.90
90916	NDS	MTP	752	0.97	32.1	1006.5	0.42	1.11	2.14	1.89
80516	FDGS	WBT	658	0.97	38.9	1092.3	0.69	0.20	1.31	2.86
81016	FDGS	WBT	706	0.97	38.4	1173.5	0.75	0.26	2.41	2.88
81216	FDGS	MTP	727	0.97	23.7	692.7	1.04	0.47	3.11	2.62
81616	FDGS	MTP	858	0.98	35.4	1401.6	0.32	0.19	1.63	2.94

Table A3. Chamber loading for each stove type at the start of the batch configuration. ΔCO and ΔCO_2 are background corrected. OA loading is as measured by the ACSM and corrected for the lens transmission (Sec. A2). The BC loading was measured by PAX using a MAC of 3.33 m^2 g^{-1}. The aged OM:OC ratio was estimated using the Improved-Ambient method[15–17] based on aged f_{44} measured during batch F-OFR sampling.

Test ID	Stove Type	Test Protocol	ΔCO (ppm)	ΔCO2 (ppm)	OA Loading (μg m^{-3})	BC Loading (μg m-3)	Aged OM:OC Ratio
62916	TSF	WBT	11.6	195.1	779.7	111.1	2.26
71916	TSF	WBT	13.0	168.9	1319.1	83.5	2.06
72916	TSF	MTP	12.6	147.5	685.5	96.0	2.09
80316	TSF	MTP	9.7	133.4	305.8	63.7	2.27
70716	Chulika	WBT	4.9	136.5	133.3	125.4	2.55
72216	Chulika	MTP	6.7	150.8	284.2	202.1	2.50
72616	Chulika	MTP	7.1	140.3	219.9	150.4	2.44
82516	Chulika	WBT	3.4	132.1	135.2	121.9	2.85
80516	Philips	WBT	3.7	111.9	147.9	58.0	2.97
81016	Philips	WBT	3.0	107.0	119.5	83.0	3.20
81216	Philips	MTP	4.3	105.8	183.1	61.5	3.05
81616	Philips	MTP	3.2	149.6	147.1	46.7	3.10

Figure A1. Cookstove models. (L to R) Three stone fire, NDS, FDGS

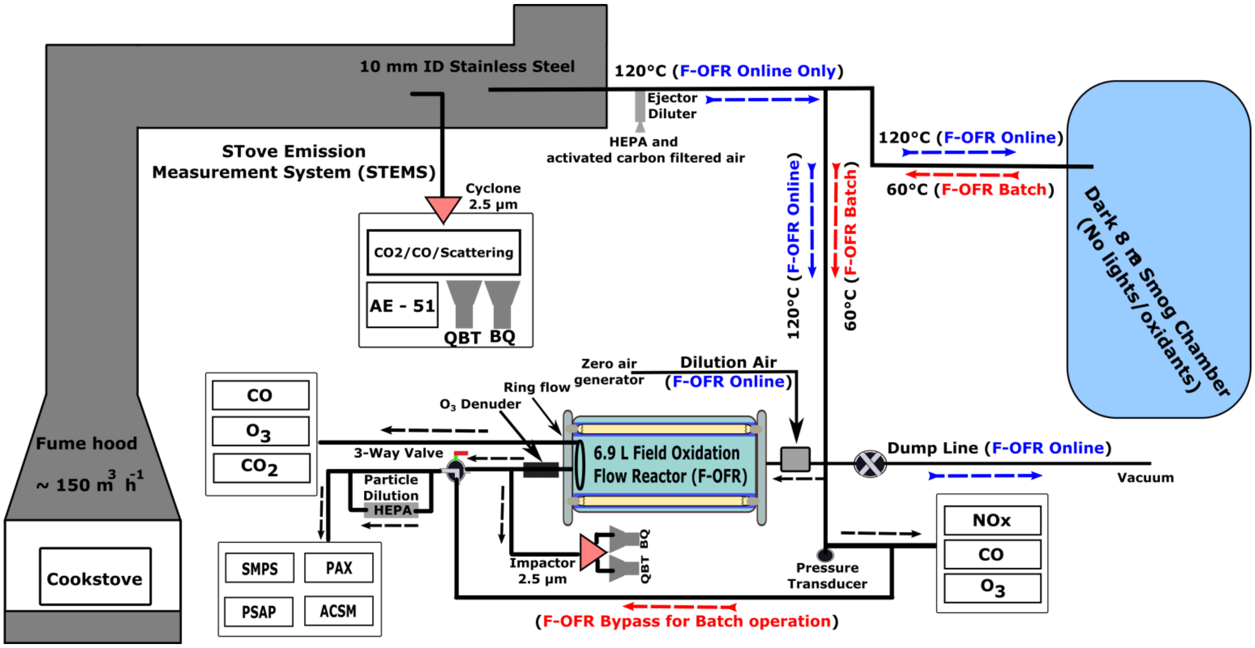

Figure A2. Experimental setup of online (blue arrows show sample path) and batch (red arrows show sample path) sampling configurations.

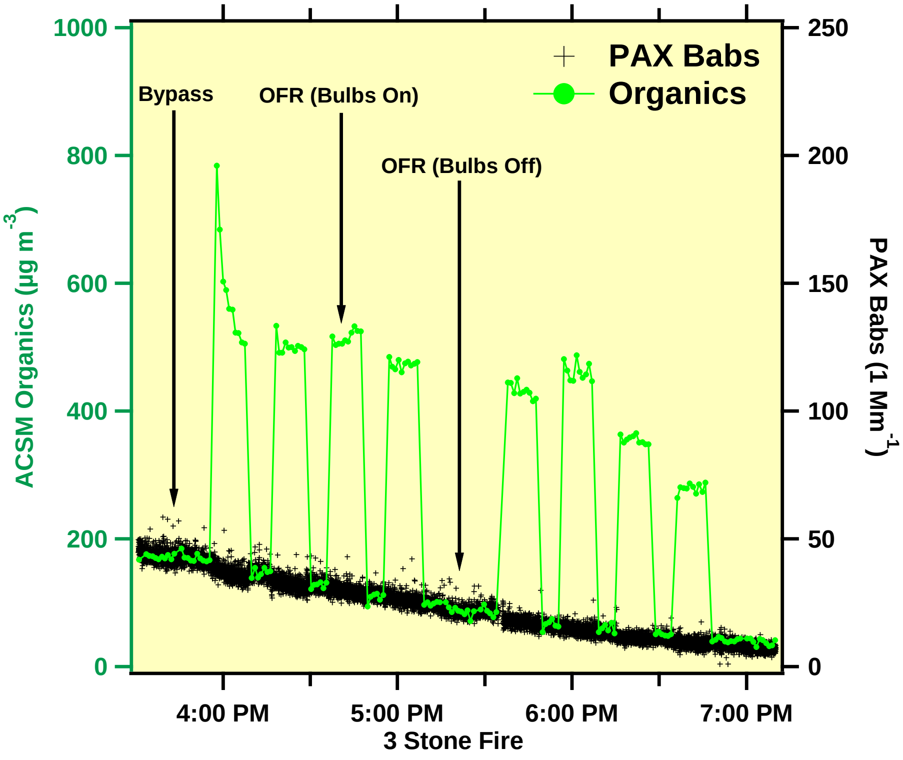

Figure A3. A time series of organics (ACSM) and absorption (PAX) from a three stone fire during batch configuration (07/19/2017). Bypass, OFR (bulbs on), and OFR (bulbs off) sampling are indicated by an arrow to demonstrate the degree of enhancement. Also shown are similar decay rates of absorption and organics over time in the chamber.

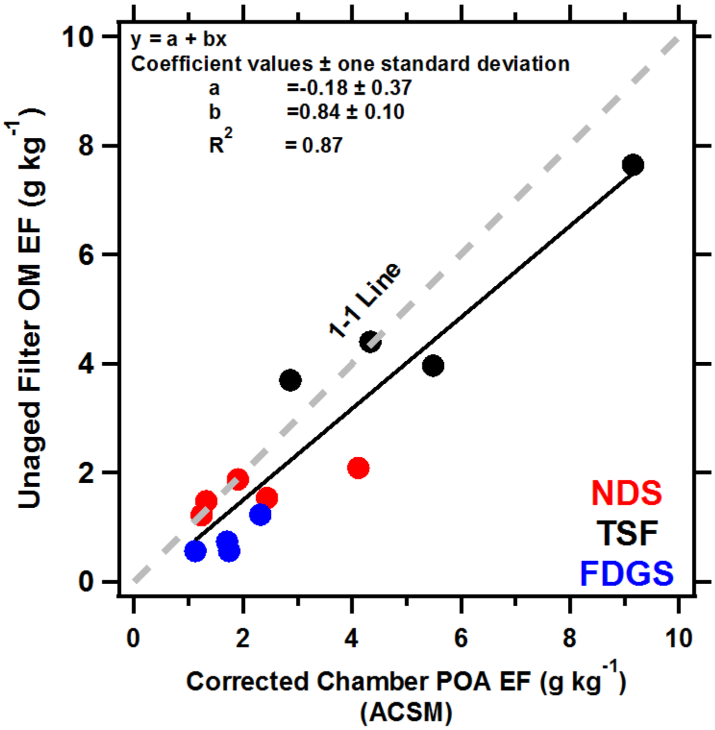

Figure A4. Comparison of online and batch configuration measurements of unaged Filter OM EF collected during the online configuration and the unaged chamber POA EF collected during the batch configuration with corrections discussed in section A2 applied.

Figure A5. Panel A-C shows OA enhancement for each OH exposure (faded points) and averaged by OH exposure ± 1 STE (dark points) for each cookstove. Solid line represents the first pass (earliest) at the range of bulb settings and the dashed line represents the second pass (latest) of equivalent bulb settings during batch sampling. Minimal difference between the first pass and second pass OA enhancement at similar OH exposure demonstrates a consistent absolute enhancement despite diminishing chamber POA concentrations. This suggests that vapor wall loss during the course of these experiments had minimal influence of SOA production during the course of batch sampling. Panel D is a comparison of aged OA EF measured by the ACSM during the online configuration and the chamber aged OA EF measured by the ACSM during the batch configuration at similar OH exposures. OA EF measured during batch is absolute enhancement + POA at $batch_{t=0}$.

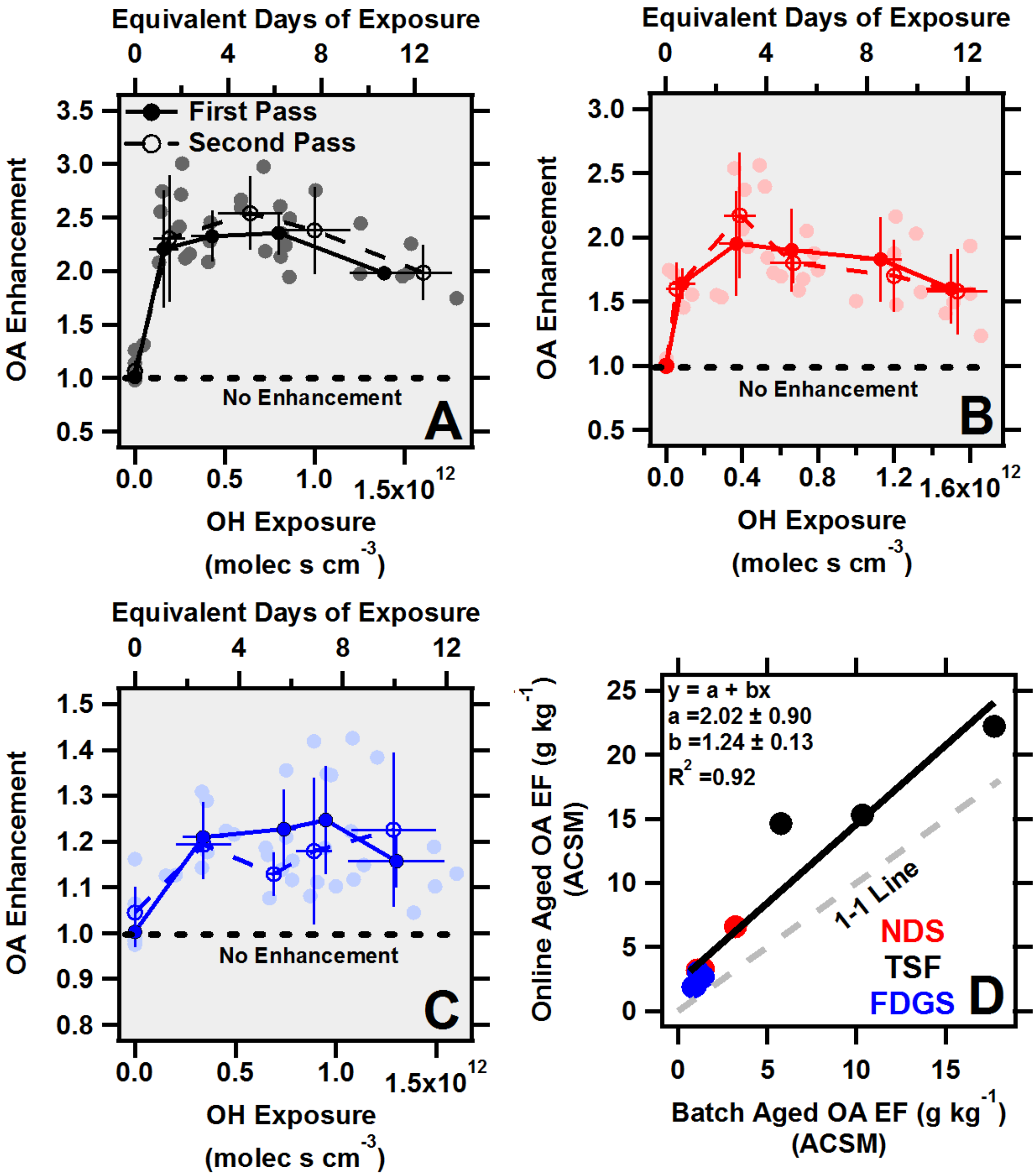
Equivalent Days of Exposure
0
4
8
12
OA Enhancement
3.5
3.0
2.5
2.0
1.5
1.0
0.5
First Pass
Second Pass
No Enhancement
A
0.0
0.5
1.0
1.5x10^12
OH Exposure
(molec s cm^-3)
Equivalent Days of Exposure
0
4
8
12
OA Enhancement
3.0
2.5
2.0
1.5
1.0
0.5
No Enhancement
B
0.0
0.4
0.8
1.2
1.6x10^12
OH Exposure
(molec s cm^-3)
Equivalent Days of Exposure
0
4
8
12
OA Enhancement
1.5
1.4
1.3
1.2
1.1
1.0
0.9
0.8
No Enhancement
C
0.0
0.5
1.0
1.5x10^12
OH Exposure
(molec s cm^-3)
Online Aged OA EF (g kg^-1)
(ACSM)
25
20
15
10
5
0
y = a + bx
a =2.02 ± 0.90
b =1.24 ± 0.13
R^2 =0.92
1-1 Line
NDS
TSF
FDGS
D
0
5
10
15
Batch Aged OA EF (g kg^-1)
(ACSM)

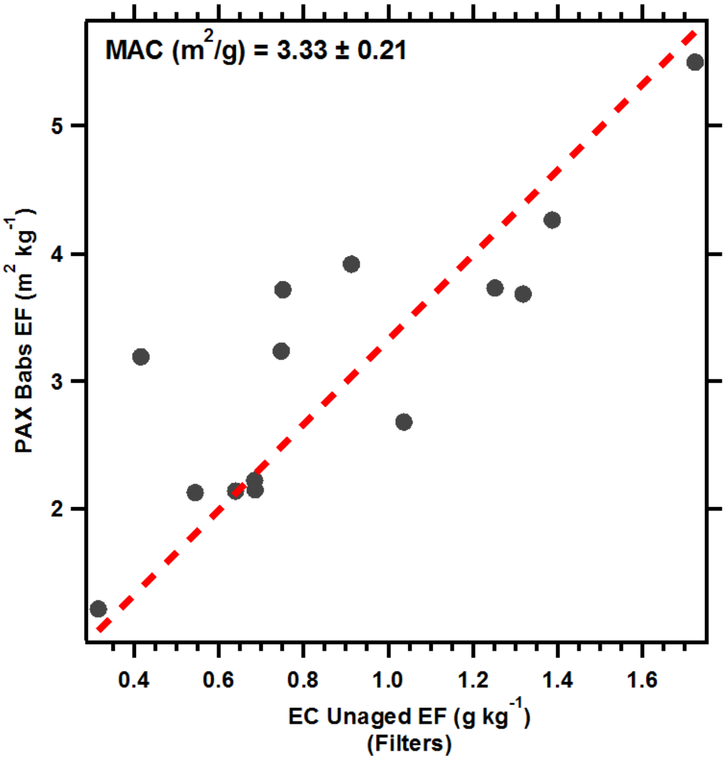

Figure A6. Calculation of the Mass Absorption Cross-Section (MAC) used to determine black carbon (BC) mass concentrations from absorbance. Unaged EC EF determined from OC/EC analysis of primary filters in the STEMS plotted against absorption EFs of unaged emissions during bypass batch sampling measured by the PAX (870nm). Absorption in the smog chamber was corrected for the loss of particles to the chamber walls during the burn duration on a per test basis.

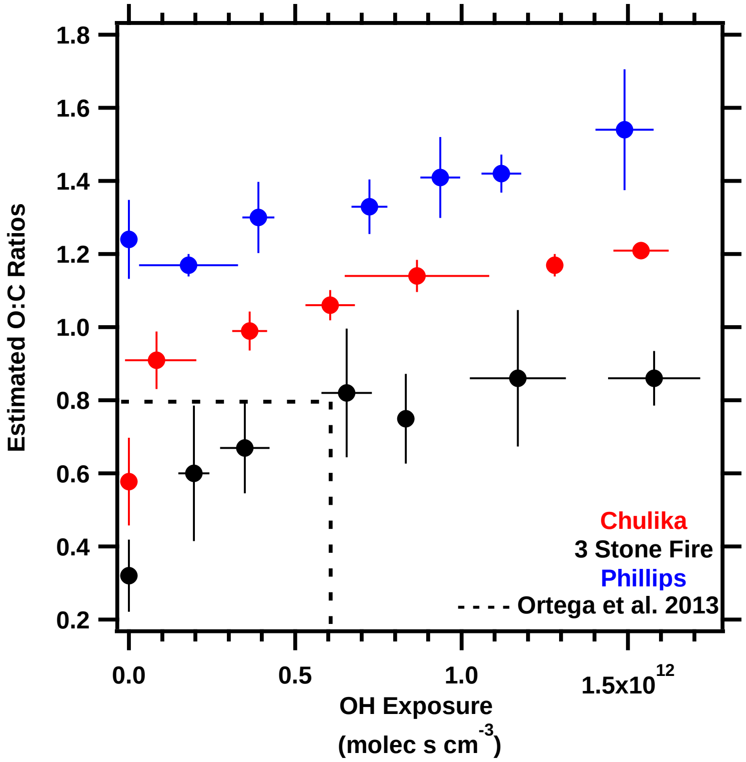

Figure A7. Estimated O:C ratios, using the Improved-Ambient' parameterization of f43 and f44 measured during batch sampling[15–17] across a range of OH exposures for each stove type. O:C ratios are averaged for each stove type by OH exposures binned by approximately two equivalent days of exposure. The dashed line indicates the maximum OH exposure and O:C ratios observed by Ortega et al. at Flame-3.

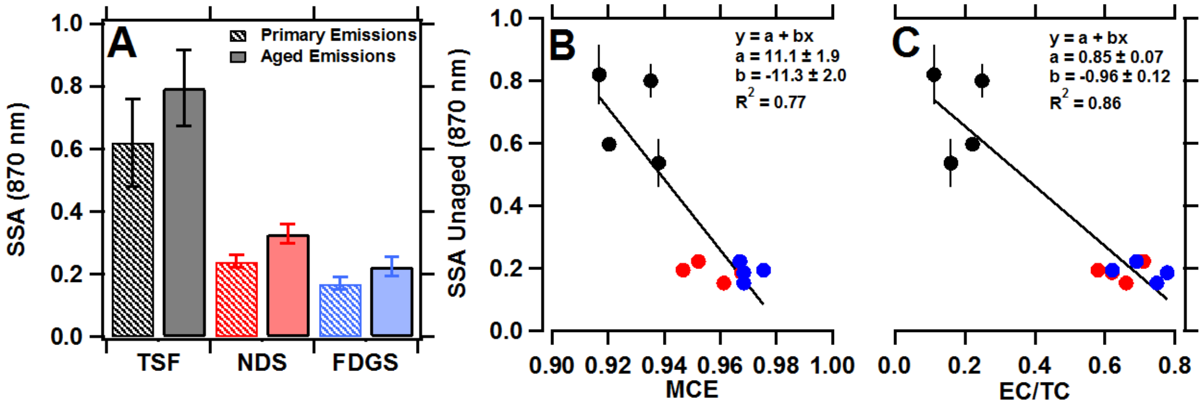

Figure A8. Effect of aging and combustion on optical properties shown by (a) unaged SSA and peak SSA after aging averaged by cookstove type after aging at 870 nm during batch configuration, (b) unaged SSA decreasing with increasing combustion efficiency, and (c) unaged SSA decreasing with increased EC.

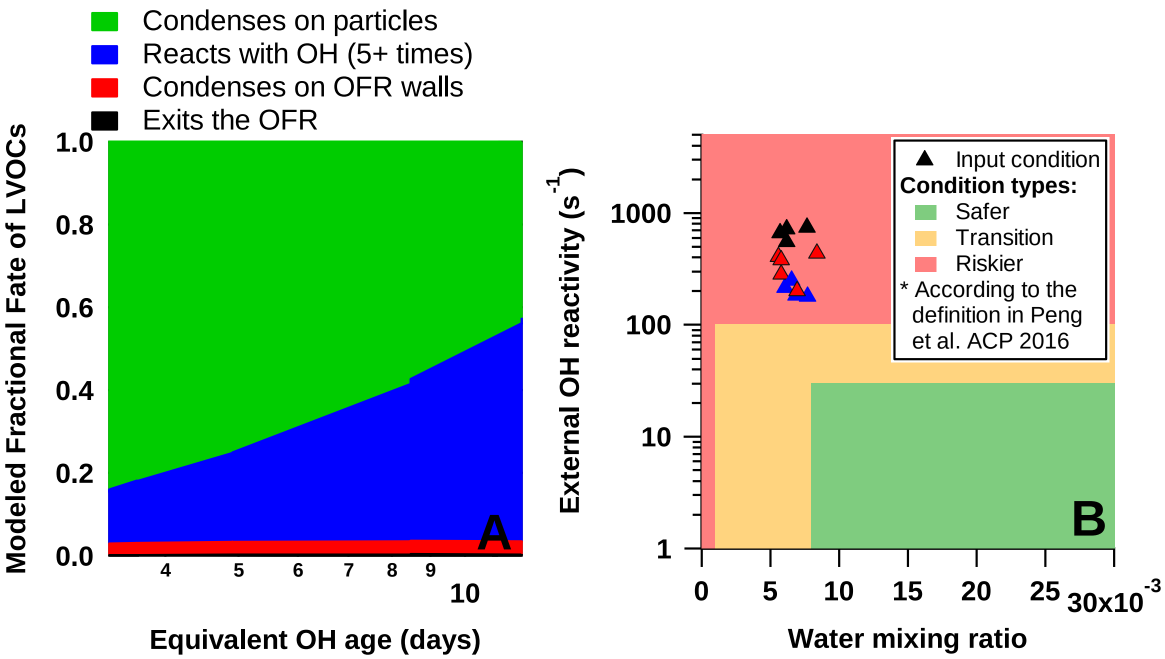

Figure A9. F-OFR modeling of: (a) the fractional fate of LVOC vapors in the reactor due to either 1) condensation on to particles 2) reacting with OH radicals 5+ times 3) condensing on to the walls of the reactor or 4) exiting the OFR, showing that condensation on particle or 'destruction' via repeated OH reactions are likely the two dominant LVOC fates under our experimental conditions[24], and (b) the external OHR and water mixing ratio of the sampled air stream for all the experiments here. This shows that the oxidation chemistry in the reactor is not in the most atmospherically relevant range, and so subsequent experiments should be run at more dilute, moist conditions (lower OHR, higher water mixing ratio)[25].

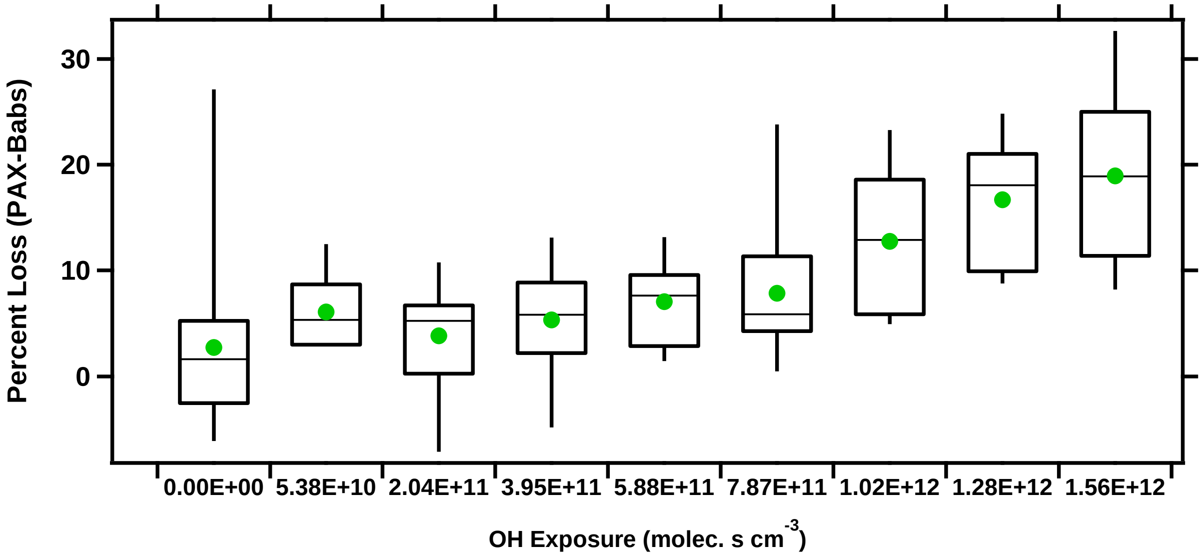

Figure A10. Box plots for percent loss of PAX-measured absorption in the F-OFR as a function of OH exposure (a proxy for bulb intensity). Loss ratio based on measurements via bypass and F-OFR during batch sampling at various OH exposures. Boxes represent interquartile range, whiskers indicate 5th and 95th percentiles and horizontal line in the box is the median. Average percent loss for each average OH exposure binned by approximately 1.5 equivalent days of aging is shown by a green dot.

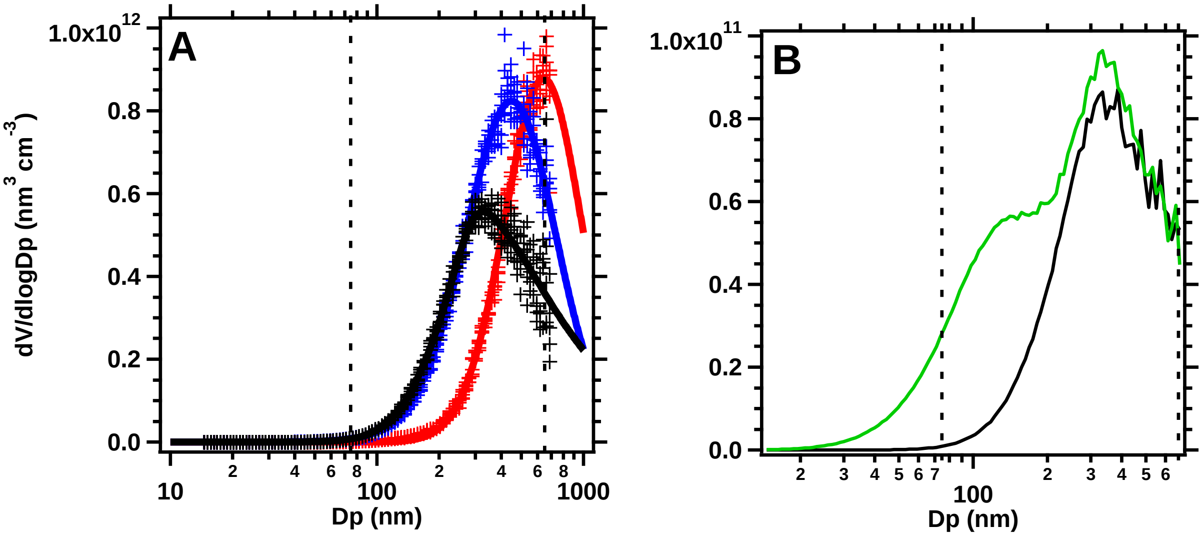

Figure A11. Representative SMPS particle volume distributions measured for the various stove options. Also shown is the ACSM lens transmission window (dashed lines): (a) bypass scans for each cookstove model (Chulika diluted by a factor of 6) and fitted to determine amount of volume outside the ACSM lens transmission (b) aged emissions (green) from the TSF (black) to demonstrate mass formation is predominantly occurring within the ACSM detection window.

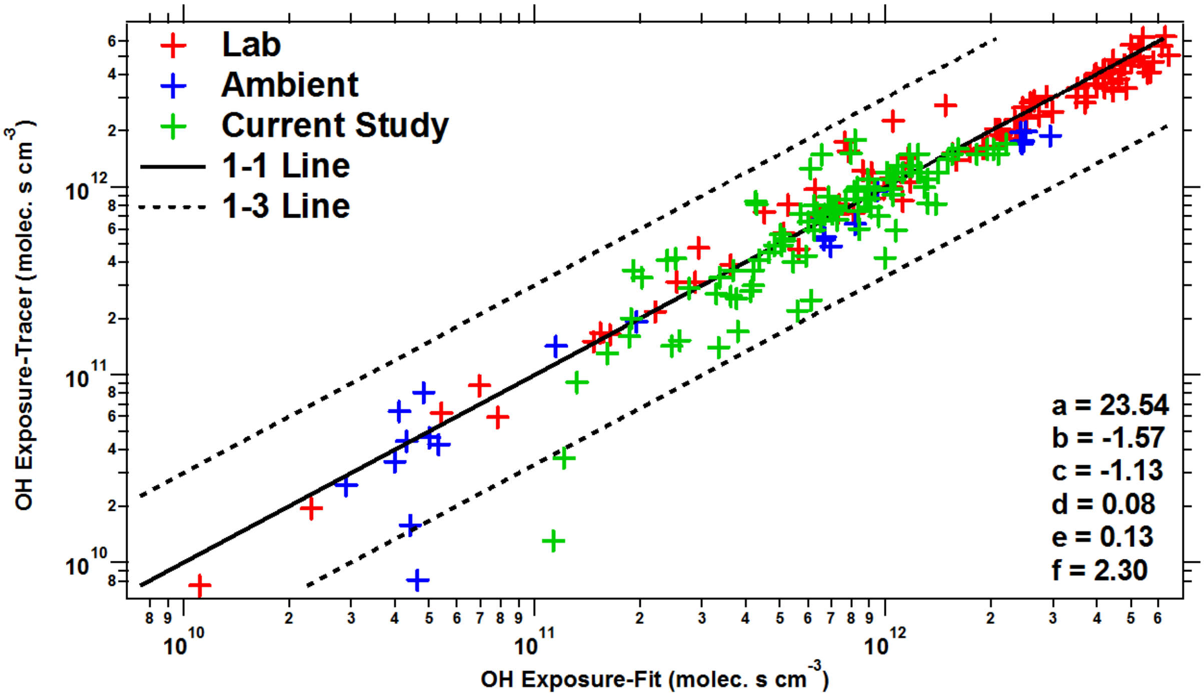

Figure A12. Comparison of OH exposure estimated using a CO tracer against a model prediction (discussed in Section SA3) during laboratory characterization experiments (red points), ambient measurements (blue points), and the current study (green points). Dashed lines are the 1-3 lines and the solid line is the 1-1 line.

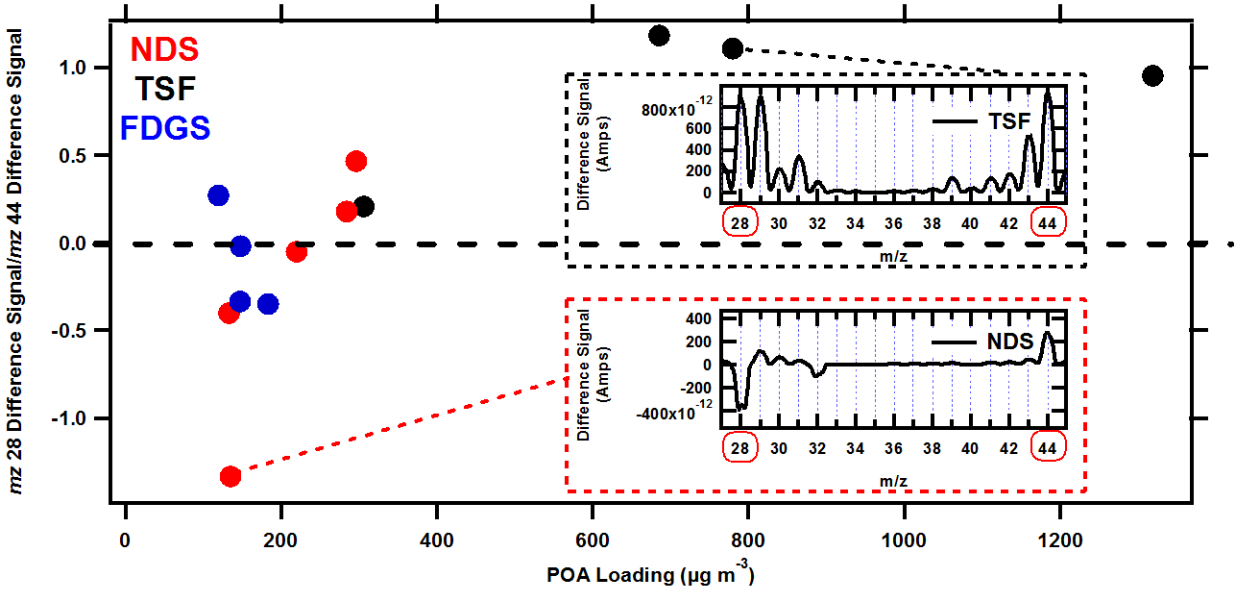

Figure A13. ACSM mass spectra for a full test (difference = unfiltered minus filtered spectra) showing signals between *m/z* 28 and 44 from test number TSF-062916 and NDS-082516 with loadings of ~779.7 µg m^{-3} and 135.2 µg m^{-3}. This is clear evidence of a substantial particle-phase signal at m/z 28. This was visible in TSF-062916 and other TSF tests, but high noise levels precluded us from consistent quantification of OA contribution at m/z 28 across all stove tests.